8-2016

Evaluation of the Potential for Weld-Related Cracking in Cast 20Cr-32Ni-1Nb Heat-Resistant Stainless Steel

John William Bohling
University of Tennessee, Knoxville, jbohling@vols.utk.edu

To the Graduate Council:

I am submitting herewith a thesis written by John William Bohling entitled "Evaluation of the Potential for Weld-Related Cracking in Cast 20Cr-32Ni-1Nb Heat-Resistant Stainless Steel." I have examined the final electronic copy of this thesis for form and content and recommend that it be accepted in partial fulfillment of the requirements for the degree of Master of Science, with a major in Materials Science and Engineering.

Carl D. Lundin, Major Professor

We have read this thesis and recommend its acceptance:

Hahn Choo, Carl J. McHargue

Accepted for the Council:
Carolyn R. Hodges

Vice Provost and Dean of the Graduate School

(Original signatures are on file with official student records.)

Evaluation of the Potential for Weld-Related Cracking in Cast 20Cr-32Ni-1Nb Heat-Resistant Stainless Steel

A Thesis Presented for the

Master of Science

Degree

The University of Tennessee, Knoxville

John William Bohling

August 2016

To my parents,

Mark and Sandra Bohling

Acknowledgements

I would like to thank my major advisor, Dr. Carl Lundin, for his guidance and advice over the course of this project. I am also thankful for my patient committee members, Dr. Hahn Choo and Dr. Carl McHargue.

I would like to thank my fellow graduate students in the Materials Joining Group over the years, in particular D. Joshua Burgess, Max Trent, and Maneel Bharadwaj, for sharing their knowledge and experience and for our stimulating discussions on metallurgy and other sundry topics. I am also grateful to the Materials Properties Council under the direction of Dr. Martin Prager and to the Center for Materials Processing, directed by Dr. Claudia Rawn through the Department of Materials Science and Engineering at the University of Tennessee, Knoxville, for providing funding to support this work.

S.D.G.

Abstract

Steam reforming of hydrocarbons is an important process for the production of hydrogen for industrial needs, such as ammonia synthesis. Due to the high temperature conditions (700 °C–900 °C), reformer furnace components require materials with excellent creep properties and thus highly alloyed austenitic stainless steels are typically employed. For reformer outlet manifolds, a cast, heat-resistant stainless steel with the composition 20Cr-32Ni-1Nb (ASTM A351 Grade CT15C) is widely used. However, after service exposure this alloy exhibits problems with liquation cracking in the base metal heat-affected zone (HAZ) during repair welding. In the work presented herein, two heats of material from centrifugally-cast manifold components were evaluated to quantify the potential susceptibility to HAZ liquation cracking. The weldability of the 20Cr-32Ni-1Nb materials was evaluated using the Gleeble® hot ductility test to determine the on-heating and on-cooling ductility (percent reduction in area) at various temperatures after exposure to a simulated welding thermal cycle. The as-received materials and selected hot ductility samples were characterized using optical light microscopy (OLM) and

scanning electron microscopy (SEM) with energy dispersive x-ray spectroscopy (EDXS) to correlate the hot ductility behavior with microstructural characteristics.

Both 20Cr-32Ni-1Nb heats showed similar hot ductility behavior when tested (*i*) on-heating, and (*ii*) on-cooling from the measured zero ductility temperature (ZDT) of 1302 °C (2375 °F). The hot ductility curves revealed that both materials exhibited a poor recovery of on-cooling ductility (Class C3 based on the Nippes criteria) after exposure to the ZDT, with a noticeable zero ductility range (ZDR) and a low ductility recovery rate (DRR) on the order of 20%. The microstructural evaluation revealed that the loss of on-heating and on-cooling ductility was a result of liquation along the interdendritic boundaries. EDXS analysis did not reveal the presence of significant amounts of Ni-Nb-Si enriched phases adjacent to the niobium carbides. The observed liquation along the interdendritic boundaries was attributed to constitutional liquation of niobium carbides which were present in the boundary regions. Based on these findings, the two 20Cr-32Ni-1Nb heats are sensitive to HAZ liquation cracking when exposed to a thermal cycle as would be encountered in repair welding.

Table of Contents

List of Tables

List of Figures

List of Abbreviations

BSE back-scattered electron

DRR ductility recovery rate

DRT ductility recovery temperature

EDXS energy dispersive x-ray spectroscopy

HAZ heat-affected zone

OES optical emission spectroscopy

OLM optical light microscopy

SE secondary electron

SEM scanning electron microscopy

SMAW shielded metal arc welding

ZDR zero ductility range

ZDT zero ductility temperature

Chapter 1

Introduction

Steam reforming of hydrocarbons is an important industrial process for the production of hydrogen gas either as an end product or as an input for other processes such as ammonia synthesis and petroleum hydrocracking. In the steam reforming process, a hydrocarbon feedstock is reacted with steam in the presence of a catalyst to yield hydrogen gas and byproducts according to the following reactions [1]:

$$\mathrm{C}_n\mathrm{H}_m + n\,\mathrm{H_2O} \longrightarrow n\,\mathrm{CO} + \left(n + \frac{m}{2}\right)\mathrm{H_2} \quad (-\Delta H^0_{298} < 0) \tag{1.1}$$

$$\mathrm{CO} + \mathrm{H_2O} \rightleftharpoons \mathrm{CO_2} + \mathrm{H_2} \quad (-\Delta H^0_{298} = 41.2\,\mathrm{kJ\ mol^{-1}}) \tag{1.2}$$

$$\mathrm{CO} + 3\,\mathrm{H_2} \rightleftharpoons \mathrm{CH_4} + \mathrm{H_2O} \quad (-\Delta H^0_{298} = 206.2\,\mathrm{kJ\ mol^{-1}}) \tag{1.3}$$

Most commonly, methane (CH_4) in the form of natural gas is the preferred feedstock, although heavier hydrocarbons such as propane, naphtha, and heptane

can be used depending upon availability and cost [1, 2]. In the above reactions, steam functions as an oxidizing agent to break apart the hydrocarbon; in some variants of the process, air is also added as a further oxidizer. The catalyst is typically nickel-based on an oxide substrate [1].

By adjusting the process conditions (exit temperature and amount of steam), the equilibria of the reforming reactions 1.1–1.3 can be modified to favor certain products and thereby adjust the composition of the product gas. For example, for ammonia synthesis which is one of the largest industrial consumers of hydrogen, the typical desired process conditions are 3.3 MPa (480 psi) exit pressure, 800 °C (1472 °F) exit temperature, and a steam to carbon ratio of 3.7 [1] to minimize the methane content in the product. Considering that reaction 1.1 is endothermic while reactions 1.2 and 1.3 are exothermic, under the process conditions just listed (for minimizing methane) the overall reaction is endothermic and thus external heating is required. The necessary heat is supplied by enclosing the reaction apparatus in a *reformer furnace*.

An illustration of a typical reformer furnace is shown in Figure 1.1. The furnace is a tubular reformer design, in which the feedstock stream (e.g. containing natural gas and steam) is fed simultaneously through a series of identical, externally heated tubes which contain the catalyst material. These tubes are visible in Figure 1.1 in a vertical arrangement, with the burners installed on the sides of the furnace walls. The inlet side where the preheated feedstock enters the tubes is at the top of the furnace, with the hot product gas mixture collected at an outlet

manifold at the bottom of the furnace, consisting of “hot side” header, tee, and reducer ("cone") which connects to a refractory-walled transfer line. Through the transfer line, the product gas flow is directed to a waste heat recovery boiler which generates high-pressure steam to be used in the reformer [1]. A photograph of another furnace is shown in Figure 1.2 [3] in which the outlet pigtails (from the reformer tubes), the outlet header and tee, and the cone are clearly visible.

Because high exit temperatures maximize the yield of hydrogen from the reformer [2], typical temperatures are in the range of 700 °C–900 °C (1300–1650 °F) on the outlet side of the reformer furnace. Thus, the reformer tubes and outlet manifold require materials possessing excellent creep performance in addition to resistance to carburization and oxidation. The traditional choice for reformer tubes was centrifugally cast HK-40 (20Cr-25Ni) alloy [1], although this has been supplanted by other alloys such as the HP-Modified alloys (25Cr-35Ni) due to higher creep strength [4]. For outlet manifold components, Alloy 800, HU-40 (19Cr-39Ni), and HK-40 have been used previously [5]. The HU-40 and HK-40 alloys were implemented because they offered higher creep strength than Alloy 800, but they were discovered to have problems either with excessive thermal gradients across the wall thickness (for HU-40), which was the same problem as originally experienced with Alloy 800, or with unacceptable loss of ductility after long-term service exposure (HK-40) [5, 6]. To increase the ductility after service exposure while maintaining high creep strength, a cast heat-resistant stainless steel with the nominal composition of 20Cr-32Ni-1Nb was developed [6]. This alloy,

which is specified as Grade CT15C in ASTM A351 [7], has similar creep strength to HK-40 [5] with improved ductility after service-exposure.

Despite these improvements over traditional alloys, over the years industry has become aware [8] that the 20Cr-32Ni-1Nb alloy exhibits significant issues when it is subjected to repair welding after service exposure. These issues manifest primarily as cracking occurring in the base metal heat-affected zone (HAZ), for example as reported by Hoffman and Colwell [9]. The cracking occurrences are not alleviated by changes to welding procedures, such as utilizing a more ductile filler metal, but rather are only prevented by high-temperature solution annealing (> 1093 °C (2000 °F)) of the service-exposed material prior to welding. Thus the cracking issues are directly related to the microstructural changes which occur under service conditions, i.e. the high temperature environment of 700 °C–900 °C (1300–1650 °F). The objective of the current work is to evaluate the weldability of service-exposed 20Cr-32Ni-1Nb material, utilizing a well-established test method for characterizing the weldability of alloys (the Gleeble® hot ductility test), and to relate the hot ductility results to observed microstructural characteristics.

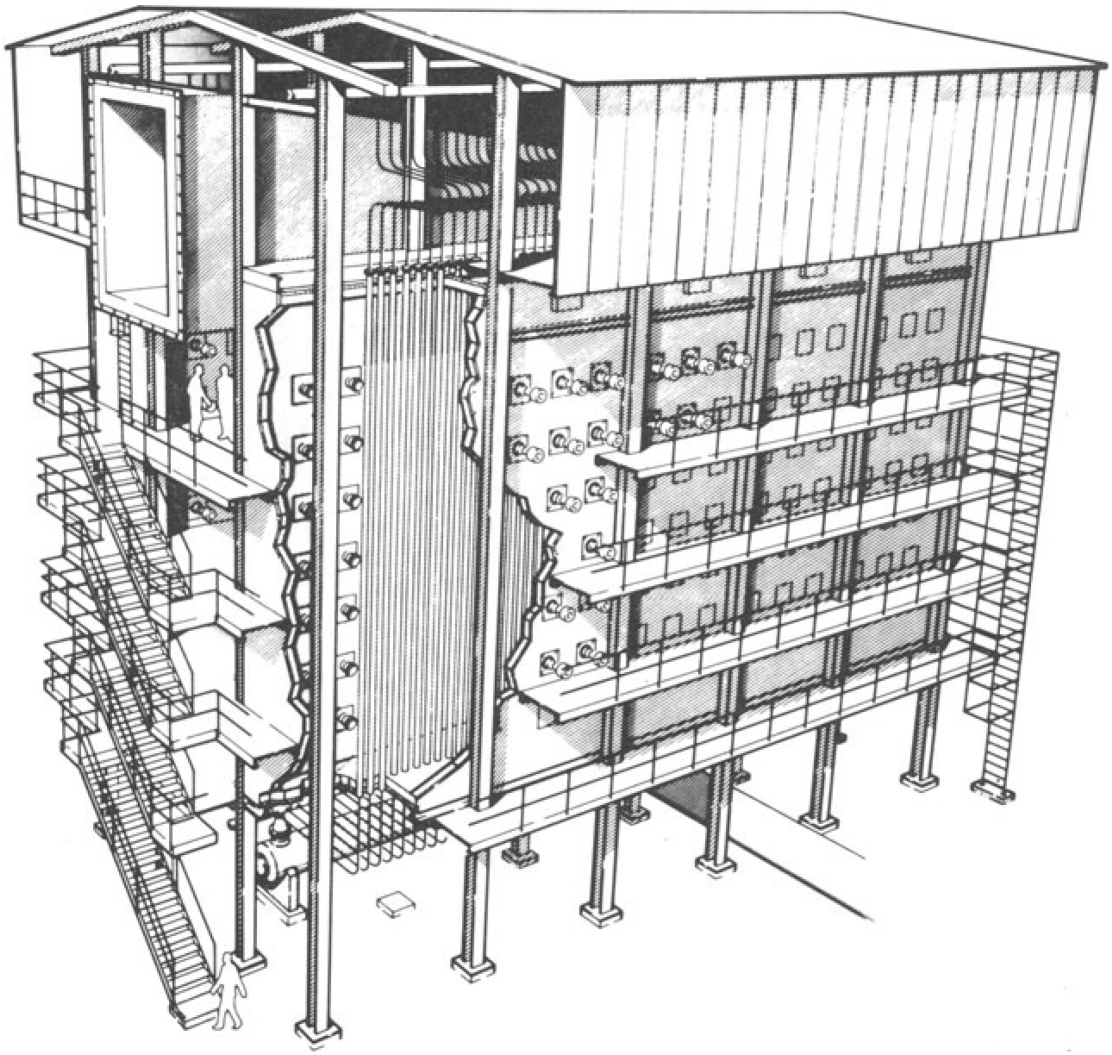

Figure 1.1: Illustration of a typical reformer furnace. The reformer catalyst tubes are arranged vertically, with side-mounted burners on both walls. The pre-heated feedstock gas mixture enters the tubes from the top and the product gas is collected in an outlet manifold at the bottom of the furnace. From Rostrup-Nielsen [1, Fig. 9].

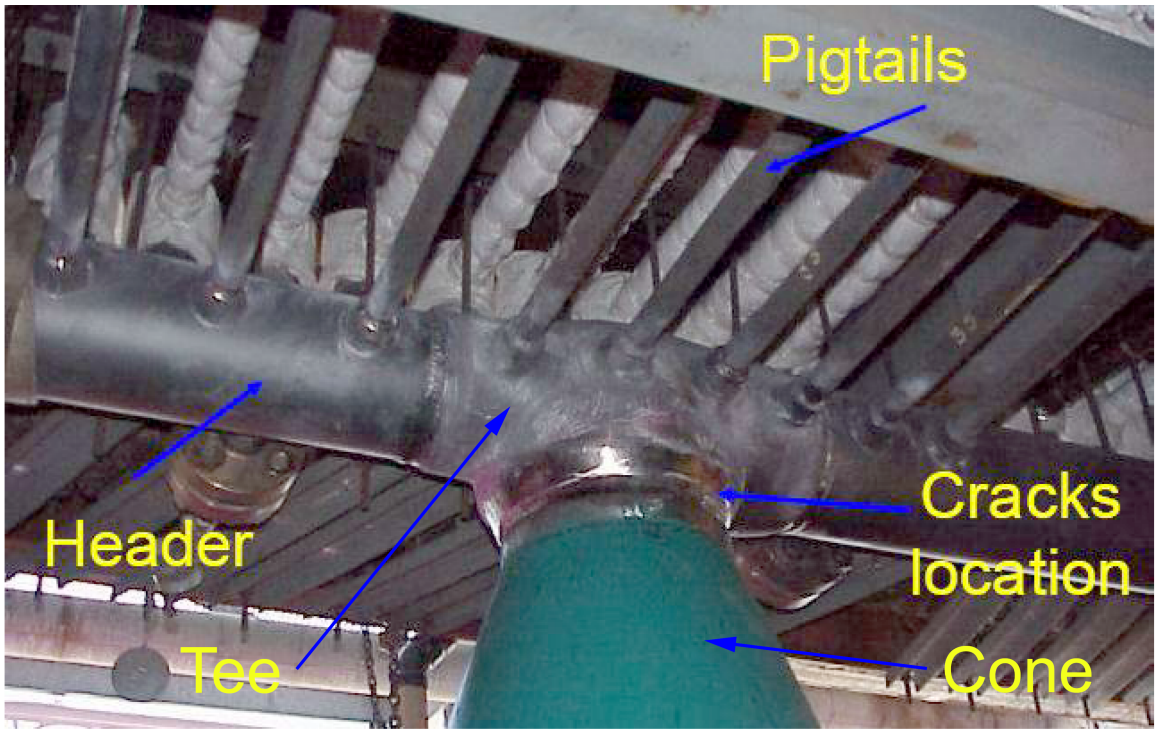

Figure 1.2: Photograph of the outlet side of a reformer furnace, showing the outlet pigtails from the reformer catalyst tubes and the outlet header, tee, and cone which connect to the refractory-lined transfer system. From Penso and Mead [3].

Chapter 2

Literature Review

2.1 Cast Heat-Resistant Stainless Steels

Cast heat-resistant stainless steels can be broadly considered as the families of cast alloys which are designed for sustained elevated temperature service above 649 °C (1200 °F) [10]. The compositions of heat-resistant stainless steels primarily fall within the categories of Fe-Cr, Fe-Cr-Ni, and Fe-Ni-Cr alloys, with varying chromium and nickel contents, e.g. as shown in Figure 2.1 for a number of alloy designations assigned by the Alloy Casting Institute. The chromium and nickel contents influence the resulting microstructure, with the Fe-Cr grades (e.g. the HA series) being predominantly ferritic [11]. Fe-Cr-Ni grades are either austenitic-ferritic (duplex) or fully austenitic depending on the particular composition and balance of chromium and nickel, while the Fe-Ni-Cr alloys are fully austenitic. Due to their significant chromium content which

results in a stable oxide layer at the surface, heat-resistant alloys exhibit good-to-excellent resistance to corrosion and oxidation in high temperature environments (e.g. carburizing, nitriding) [11]. High temperature (creep) strength varies according to microstructure, with the ferritic Fe-Cr alloys exhibiting comparatively lower strength at elevated temperatures [12] and thus are typically confined to applications requiring high-temperature corrosion resistance under moderate loading [11]; the fully austenitic heat-resistant stainless steels exhibit superior high temperature strength. The principal mechanism providing high temperature strength in heat-resistant stainless steels is the uniform precipitation of fine secondary carbides throughout the matrix [11, 12].

2.1.1 Effects of Alloying Elements

Chromium (Cr) is a principal alloying element in heat-resistant stainless steels, with typical Cr contents in the range of 10–30% as shown in the summary of various alloy designations in Figure 2.1. Chromium is added primarily for high temperature oxidation resistance which originates from the formation of a stable, adherent surface layer of chromium oxide [13]. Chromium is a strong ferrite stabilizer [14] and thus in alloys where a fully austenitic structure is desired but which may be lean in austenite-stabilizing elements (e.g. the HH series), the Cr content must be balanced carefully [12]. Chromium also combines with carbon to form a variety of carbides, with the $(Fe,Cr)_{23}C_6$ complex carbide being the primary

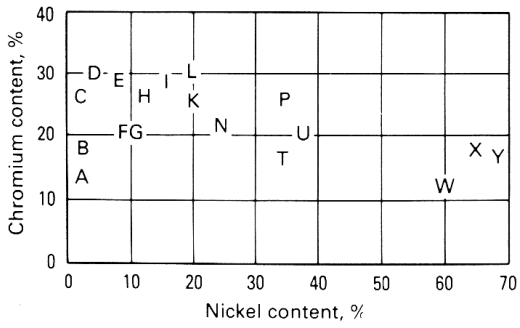

Figure 2.1: Diagram indicating chromium and nickel contents of various cast stainless steel compositions using the letter designations of the Alloy Casting Institute. Each letter is combined with a "C" prefix for corrosion-resisting alloys or a "H" for heat-resisting alloys (e.g. the designation "HT" denotes a heat-resistant alloy with 16 wt% Cr, 35 wt% Ni). From Blair [10].

type in heat-resistant stainless steels [15]. Although precipitation of Cr carbides contributes to creep strength, Cr carbides are less stable at higher temperature ranges and have a tendency to coarsen, reducing their strengthening effect [12].

In combination with chromium, nickel (Ni) constitutes the other primary alloying element in heat-resistant stainless steels. Nickel content in heat-resistant alloys varies over a wide range, 1–60% (Figure 2.1). Nickel is a strong austenite stabilizer [14] and thus sufficient addition of Ni permits fully austenitic microstructures at room temperature. Nickel is also beneficial for resistance to high temperature oxidation and carburization by promoting a stable chromium oxide layer, and thus alloys intended for higher temperature service utilize higher nickel contents [13].

The primary function of niobium (Nb) additions in heat-resistant alloys is to increase the high-temperature creep strength. Niobium combines preferentially

with carbon to form niobium carbides (NbC), which are more stable at elevated temperatures than chromium carbides with a lower tendency for coarsening [16]. In cast alloys, NbC forms as a eutectic carbide along the interdendritic boundaries [11] which contributes to improved creep performance by inhibiting grain boundary sliding [17]. Niobium carbide also forms as fine intradendritic carbides within the matrix [18], both in as-cast condition and after high temperature exposure. High niobium levels (well above the stoichiometric amount required for formation of NbC) are associated with reduced oxidation resistance [6].

Silicon (Si) is added as an intentional alloying element in heat-resistant stainless steels as a deoxidizer (typical steel-making practice) and also for the purpose of increasing the high temperature oxidation resistance [13] by improving the adhesion of the protective chromium oxide layer that forms on the surface of heat-resistant alloys. However, it has been observed that increasing silicon content is correlated with a reduction in creep strength in heat-resistant alloys [12]. Additionally, the tendencies for formation of embrittling sigma phase and for formation of Ni-Nb-Si phases (Ni-Nb silicide or G-phase) during high temperature exposure both increase as the silicon content increases [11, 19]. In cast alloys, silicon is also added to obtain good fluidity of the molten metal for improved casting quality [10].

2.1.2 High Temperature Behavior

During exposure to an elevated temperature environment, cast heat-resistant stainless steels experience a number of microstructural changes. Starting from the as-cast condition, high temperature exposure leads to the precipitation of carbides in the austenitic matrix, due to the fact that the as-cast material may retain significant carbon in solid solution [12]. The degree of precipitation is dependent on the carbon content, with higher carbon alloys exhibiting a greater extent of carbide precipitation. Additionally, the morphology of the carbides is dependent on the temperature range which initiates precipitation (at the beginning of service), e.g. initial exposure at 649 °C (1200 °F) will precipitate finer carbides than exposure at 871 °C (1600 °F) [12]. After longer duration exposure, particularly at higher temperatures (e.g. 1093 °C (2000 °F)), the carbides in the matrix will coarsen with a consequent detrimental effect on creep strength [12].

In addition to carbide precipitation and/or coarsening, high temperature exposure can result in the formation of other intermetallic phases, depending on the chemical composition. Particularly in fully or partially ferritic heat-resistant stainless steels, the intermetallic constituent sigma phase (FeCr) can form which embrittles stainless steels and reduces creep strength when located on grain boundaries [12, 15]. Of particular concern in the niobium-alloyed heat-resistant stainless steels is the potential formation of silicide phases after elevated temperature exposure; one such constituent is G-phase, which is usually

associated with a nickel and niobium-rich composition ($Ni_{16}Nb_6Si_7$) [15]. The tendency for formation of G-phase increases with increasing silicon content [19, 20]. In cast 20Cr-32Ni-1Nb heat-resistant stainless steel (ASTM A351 Gr. CT15C), the formation of Ni-Nb-Si constituents has been frequently observed after service exposure in the range of 760 °C–850 °C (1400 °F–1560 °F). The formation of silicide phases in this alloy has been associated with reduced room temperature mechanical properties [5, 21], reduced creep strength [5], and also with severe HAZ cracking problems during repair welding [9, 22].

2.2 Liquation Cracking

Liquation cracking is a type of weld-related "hot" cracking* which is associated with the formation† of liquid films along grain boundaries in the HAZ, immediately adjacent to the fusion line, as a result of a high temperature excursion during a welding thermal cycle [23]. Liquation cracking occurs at this location because the region of the HAZ immediately adjacent to the fusion line is the region which is subjected to the highest peak temperatures during welding. Although liquation cracking can occur both in the base metal HAZ and in weld metal HAZs (in the case of reheated weld metal in multi-pass weldments), only the former will be discussed here. In common with other forms of hot cracking, HAZ liquation

*"Hot" cracking occurs at high temperatures during welding, as opposed to "cold" cracking which occurs at or near ambient temperature (e.g. hydrogen related cracking).

†In contrast to solidification cracking (another form of hot cracking) in the weld deposit, wherein cracking is associated with liquid films *remaining* along the boundaries at the terminal stages of solidification.

cracking requires the simultaneous occurrence of two factors: a critical level of applied strain and a susceptible microstructure exhibiting limited ductility over a critical temperature range. The imposition of strain on the HAZ is inherent to welding, either from mechanical restraint (e.g. arising from the weld geometry or from external fixturing) or from thermal contraction during the on-cooling portion of a welding thermal cycle. Yeniscavich [24] estimated the level of thermal strain in the HAZ to be on the order of $< 1\%$, indicating that an HAZ region must exhibit essentially zero ductility for cracking to occur.

A condition of zero ductility in the HAZ originates from the formation of liquid films along the grain boundaries in the HAZ, since liquid films have very limited capability to support strain. Liquid along the grain boundaries can be formed from several sources by the high temperatures experienced in the HAZ during welding. Segregation of impurity elements and/or alloying elements (in solid solution) will occur at grain boundaries, since these regions were the last to solidify during the initial casting process and thus will have an inherently lower melting temperature than the adjacent matrix. This is especially true of cast materials where the original dendritic structure has not been disrupted by subsequent working/forming operations (as would occur for wrought materials). Another potential source of liquation is low-melting point phases which preferentially form at grain boundaries (again, due to segregation). Finally, liquid can also be formed by the mechanism of constitutional liquation as developed by Pepe and Savage [25]. Constitutional liquation is a non-equilibrium phenomenon arising from

the rapid heating rates typical of welding and can be explained in a simplified manner in relation to the schematic binary phase diagram shown in Figure 2.2. For a nominal composition C_0 which exhibits a two-phase microstructure at low temperatures, during the heating portion of a welding thermal cycle the temperature will increase to the point (T_3) where the equilibrium phase diagram predicts a single phase region and thus the secondary phase constituent will begin to dissolve. However, due to the rapid heating rate associated with welding, insufficient time is available for complete dissolution of the secondary constituent before the temperature exceeds the local melting point, in the following manner. Because the dissolution of the secondary phase must proceed by diffusion, if the diffusion rate of solute away from the secondary phase is slow, dissolution will create a concentration gradient at the interface of the secondary phase and the surrounding matrix, wherein a region of the matrix enriched in solute will exist around the particle. As the temperature continues to increase rapidly during the heating portion of the thermal cycle, the temperature will eventually exceed the local melting temperature of the enriched region (e.g. above T_e) and liquid will form. It is important to point out that in this reaction, the temperature at which liquid begins to form is well below the solidus temperatures of both the secondary constituent and the bulk matrix composition. In the case where the secondary phase exists primarily along grain boundaries (or interdendritic boundaries in a cast material), constitutional liquation of the secondary phase will produce liquid along the boundaries and thereby establish the conditions for liquation cracking.

Constitutional liquation of constituent particles in the HAZ has been observed in a number of alloy systems, e.g. liquation of Ti-rich phases in Alloy 800 [26] and liquation of niobium carbide (NbC) in Inconel 718 [27] and AISI 347 [28].

2.3 Weldability Evaluation

The term *weldability* as defined by the American Welding Society corresponds to "the capacity of [a] material to be welded under the imposed fabrication conditions into a specific, suitably designed structure performing satisfactorily in the intended service" [29]. Thus, the weldability of a material encompasses both the fabrication and in-service performance characteristics of a completed weldment. In order to evaluate these characteristics, *weldability testing* is performed to ensure that a given combination of material, weld configuration/design, and welding parameters will result in a satisfactory weldment. A number of weldability tests to evaluate susceptibility to hot cracking and liquation cracking (described in Section 2.2) have been developed and are divided into two categories: self-restraint tests and externally-loaded tests [30]. As described in Section 2.2, liquation cracking (and hot cracking in general) essentially arises from the inability of a susceptible microstructure to accommodate strain over a particular critical temperature range. In self-restraint tests, the inherent restraint of the chosen weld configuration is used as the source of strain, while in externally-loaded tests, the strain is applied by an external device or instrument. Self-restraint tests

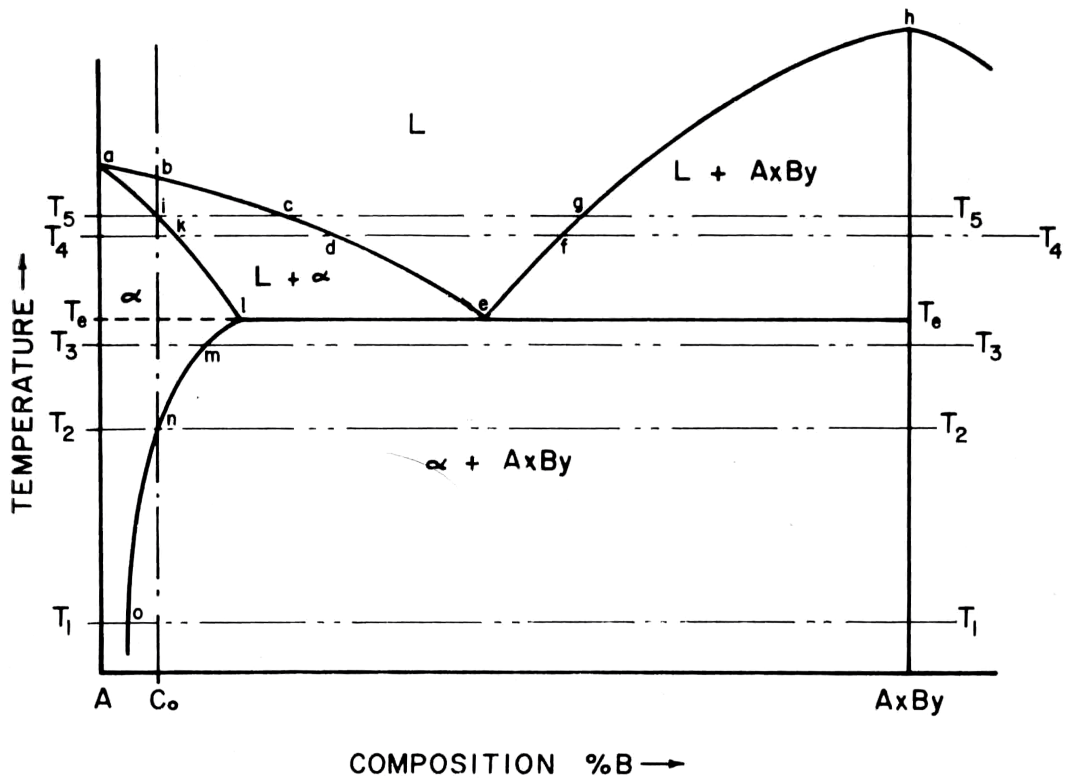

Figure 2.2: Illustration of a simple binary system in which constitutional liquation of the (AxBy) phase can occur under conditions of non-equilibrium heating (e.g. as would be typical of welding) to temperatures above T_e. From Pepe and Savage [25].

are generally considered to be a qualitative, "go/no-go" type of test in contrast to externally-loaded tests which are designed to impose strain under controlled conditions and thus are a more quantitative evaluation method that is more sensitive to variables in materials or welding conditions [30]. Among externally-loaded tests for evaluating liquation cracking, two that are widely used are the Varestraint test [31] and the Gleeble® hot ductility test [32]. The latter test method was utilized in the current study and a summary of the test method and associated evaluation criteria are described in the following sections.

2.3.1 The Hot Ductility Test

The origin of the hot ductility test can be traced back to work performed by Nippes *et al.* [33] on the measurement of the actual time-temperature history ("thermal cycle") experienced in the HAZ of various alloys during welding. Using this data as a foundation, Nippes and Savage [34] developed a device, the "Gleeble," capable of reproducing a given thermal cycle by resistively heating a sample and controlling the temperature as a function of time using an attached fine-wire thermocouple. This technique enabled the duplication of a specific region of the HAZ in a macroscopically-sized sample suitable for mechanical testing. The capabilities of the machine were expanded by adding a loading system which permitted the sample to be deformed or fractured at any point in the thermal cycle. This capability of the Gleeble® was put to use in the development

of the hot ductility test [32], in which the ductility of a particular alloy (in terms of percent reduction in cross-sectional area) is determined at various time-temperature points in the thermal cycle. The hot ductility is normally determined in two distinct modes: "on-heating" and "on-cooling." Tests to determine "on-heating" hot ductility are performed during the initial portion of the thermal cycle where the sample is heated rapidly toward the peak temperature (see Figure 2.3a). On-heating tests are typically performed at sequentially higher temperatures approaching the calculated HAZ peak temperature (usually in the vicinity of 2400°F) until a test temperature is reached where the measured on-heating ductility drops to zero (0% RA). This temperature is designated the zero ductility temperature (ZDT). Once the ZDT has been determined, "on-cooling" hot ductility tests are performed in the portion of the thermal cycle where the sample temperature is decreasing after exposure to a peak temperature corresponding to the ZDT (see Figure 2.3b). As will be discussed later, the on-cooling ductility behavior is considered the most indicative factor regarding a material's susceptibility to hot cracking. Figure 2.4 shows schematic examples of the types of curves which can be constructed using the data obtained (%RA vs. test temperature) from the on-heating and on-cooling hot ductility tests just described; important features of these curves are labeled in the plot and will be discussed in more detail in the following section. Further details regarding the history and development of the Gleeble, including references to other development papers not

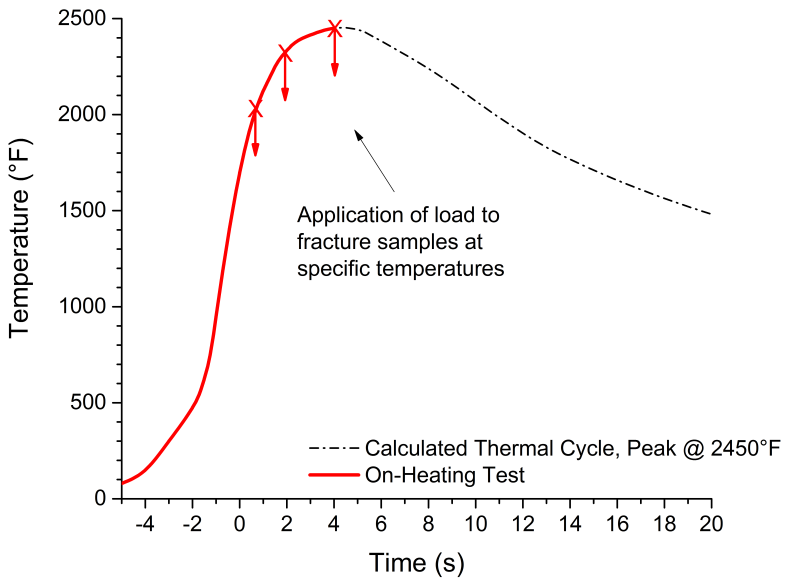

(a) On-heating hot ductility testing

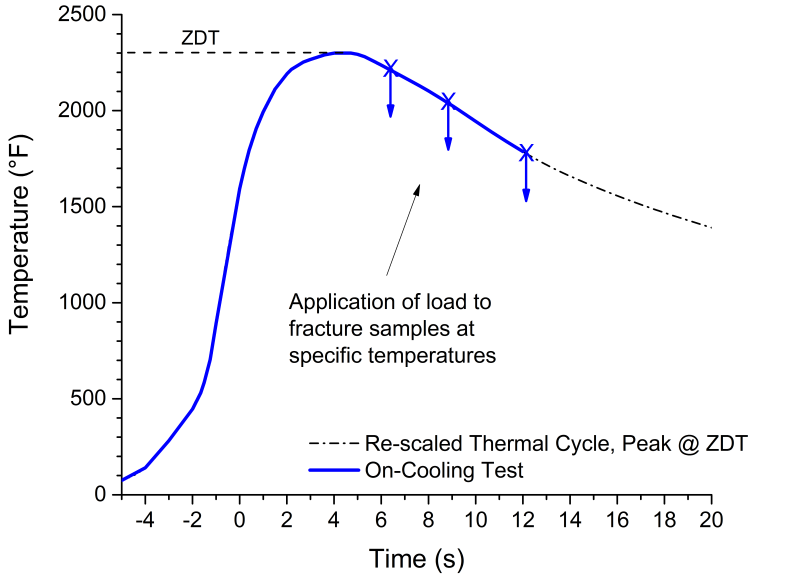

(b) On-cooling hot ductility testing

Figure 2.3: Schematic diagrams of on-heating and on-cooling hot ductility tests performed at various temperatures in a simulated welding thermal cycle.

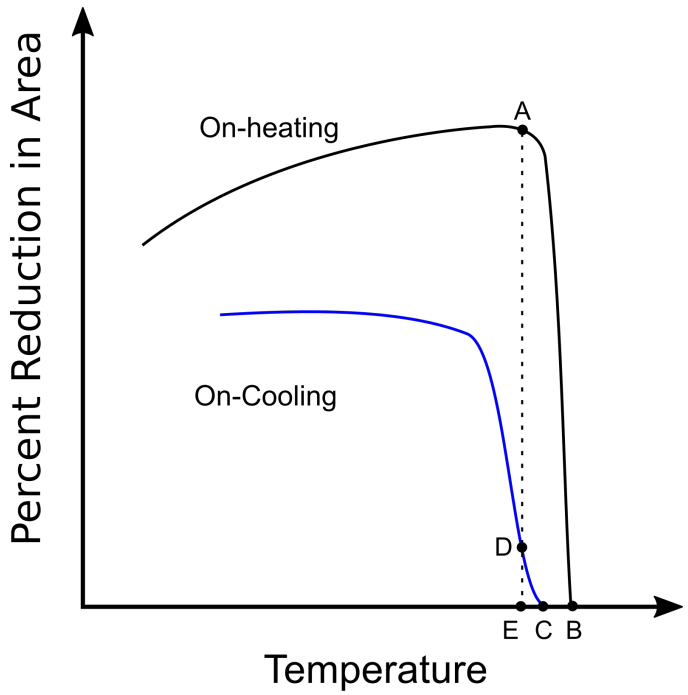

A: Rapid-Ductility-Decrease Temperature
B: Zero Ductility Temperature (ZDT)
C: Ductility Recovery Temperature (DRT)

BC: Zero Ductility Range (ZDR)
= ZDT - DRT = B - C
Ductility Recovery Rate (DRR)
= DE / AE

Figure 2.4: Schematic hot ductility curves showing on-heating and on-cooling hot ductility behavior and related evaluation criteria.

cited here and to research papers utilizing the Gleeble, can be found in the review articles by Savage [35], Lundin [36], and Lundin *et al.* [37].

2.3.2 Hot Ductility Evaluation Criteria

In one of their early studies utilizing the Gleeble hot ductility test to evaluate a number of alloys, Nippes *et al.* [38] classified the observed hot ductility responses of the various alloys into several categories, based on the shapes of the hot ductility curves: Classes H1 or H2 for the on-heating behavior and Classes C1, C2, or C3 for the on-cooling behavior. Schematic hot ductility curves illustrating the characteristics of each behavior class are shown in Figure 2.5 and a brief text description for each is provided in Table 2.1. Of the two on-heating behavior categories, Class H2 (Figure 2.5b) behavior was identified as being intrinsically sensitive to hot cracking. Class H1 behavior (Figure 2.5a) was not considered in and of itself indicative of a propensity for hot cracking and thus required the evaluation of on-cooling results to determine a material's susceptibility. With regard to the on-cooling categories, materials exhibiting Class C1 (Figure 2.5c) behavior were considered not sensitive to hot cracking. Class C2 and Class C3 behaviors (Figure 2.5d,e) were associated with a higher sensitivity to hot cracking, with Class C3 behavior indicating the greatest sensitivity. In particular, Nippes *et al.* found that those materials in the study which were known to exhibit hot cracking, based on field welding experience, exhibited Class C3

behavior with on-cooling ductility of 40% or less of the on-heating ductility. Thus, using the Nippes classification system, in most cases a material's on-cooling ductility response will be the major indicating factor regarding its hot cracking susceptibility. Materials exhibiting Class C3 on-cooling behavior with a low recovery of on-cooling ductility (0–40% of on-heating ductility) can be identified as showing the greatest susceptibility to hot cracking.

Further investigation of hot ductility test criteria was undertaken in a review by Yeniscavich [24]. One of the criteria reviewed, attributed to Nippes, was the ductility recovery rate (DRR). According to this criteria, crack-resistant materials show a rapid recovery of on-cooling ductility after exposure to the HAZ peak temperature, while the on-cooling ductility for crack-sensitive materials recovers slowly and remains low even at test temperatures well below the peak temperature. Schematic curves illustrating the DRR for crack-resistant and crack-sensitive materials are shown in Figure 2.6. Numerically, the DRR is determined by taking the ratio of the on-cooling ductility to the on-heating ductility at a specified temperature, typically the rapid-ductility-decrease temperature on the on-heating curve (the point on the curve immediately prior to the sudden drop in ductility).

Yeniscavich [24] also proposed the zero ductility range (ZDR) as an improved indicator of propensity for hot cracking. The ZDR phenomenon corresponds to a finite temperature increment below the ZDT in which the on-cooling ductility remains zero, i.e. the ductility does not immediately increase once the on-cooling test temperature is below the ZDT. The physical significance of the ZDR is

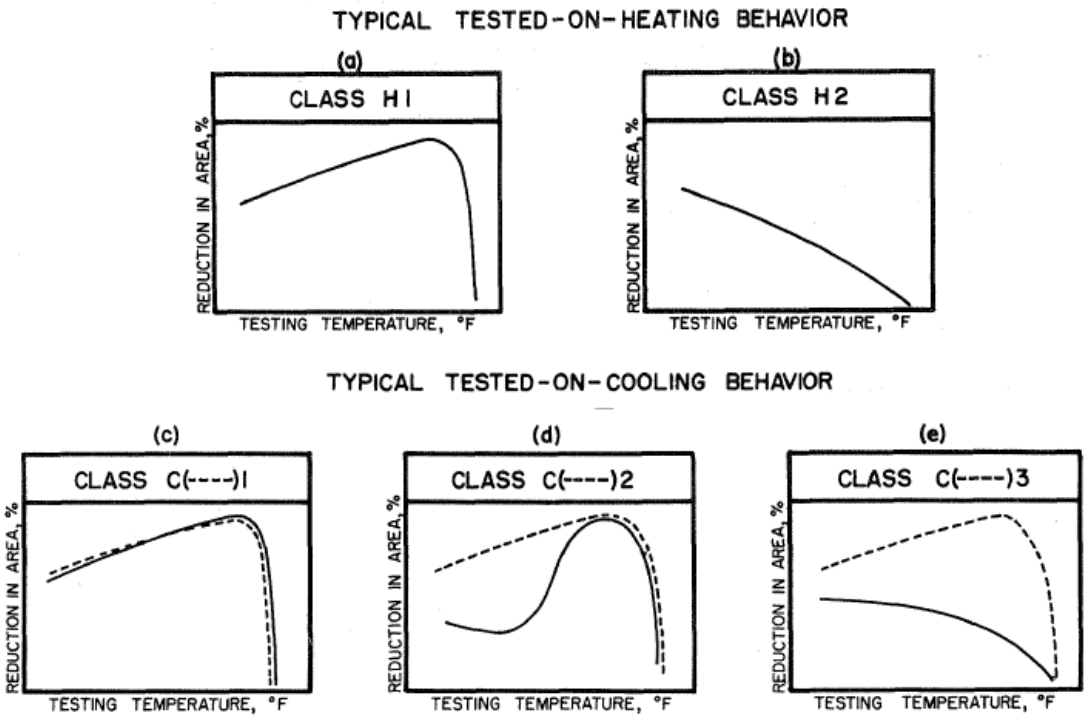

Figure 2.5: Classification of hot ductility behavior for on-heating and on-cooling tests; in (c), (d), and (e), the solid line is the on-cooling curve and the dashed line is the on-heating curve. From Nippes *et al.* [38, Fig. 66].

related to the fact that the HAZ must possess sufficient ductility to withstand the thermal strains imposed during welding, otherwise cracking will occur. Since the magnitude of these strains is small over the length scale of an HAZ, the HAZ ductility must be on the order of zero for hot cracking to be of concern. Thus, alloys which show a large ZDR (zero ductility over a wide on-cooling temperature range) are considered more vulnerable to hot cracking than alloys which show a narrow ZDR (see Figure 2.7).

Table 2.1: Classification of on-heating and on-cooling hot ductility responses based on the work of Nippes *et al.* [38]. Schematic curves for each behavior class are depicted in Figure 2.5.

Classification	**Description**
On-Heating Class H1	On-heating ductility generally increases as temperature increases, followed by a sudden loss of ductility over a relatively narrow range as the temperature increases further toward the melting point. (Figure 2.5a)
On-Heating Class H2	On-heating ductility shows a gradual decrease over a wide temperature range as the temperature increases toward the melting point. (Figure 2.5b)
On-Cooling Class C1	On-cooling ductility is the essentially same as on-heating ductility at all test temperatures. (Figure 2.5c)
On-Cooling Class C2	On-cooling ductility is the same as on-heating ductility at test temperatures of 2100°F or above, but is significantly lower at test temperatures in the range of 1800–2000°F. (Figure 2.5d)
On-Cooling Class C3	On-cooling ductility is lower than on-heating ductility at all test temperatures; severity of ductility decrease may change with on-cooling test temperature or with the peak temperature utilized for the on-cooling thermal cycle. (Figure 2.5e)

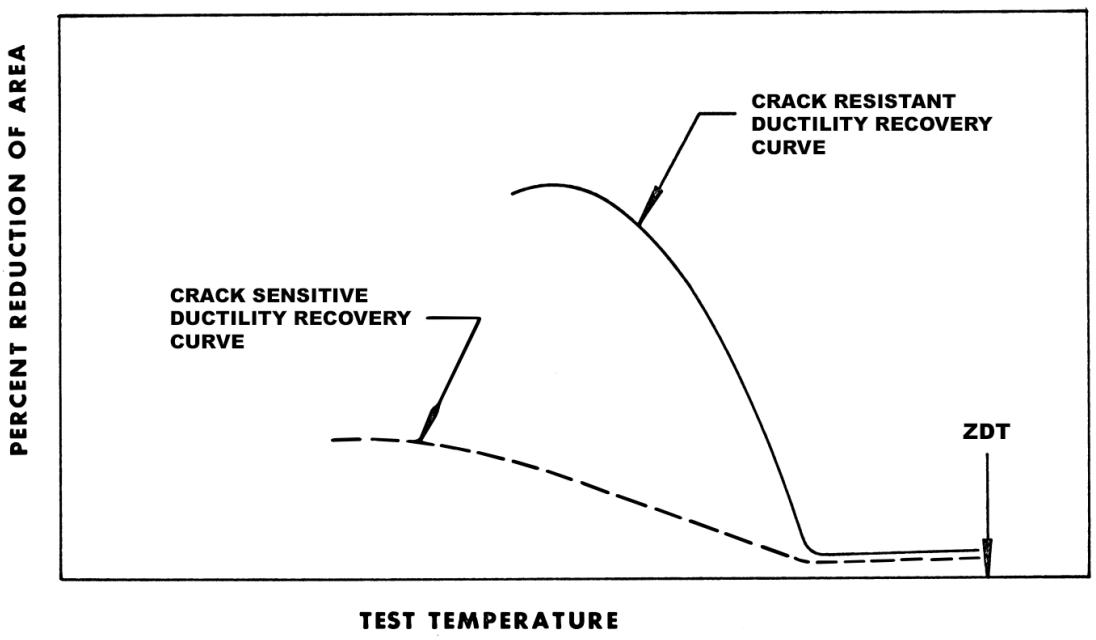

Figure 2.6: Schematic curves illustrating the on-cooling ductility recovery rate (DRR) criteria for crack-resistant and crack-sensitive materials. Adapted from Yeniscavich [24, Fig. 2]

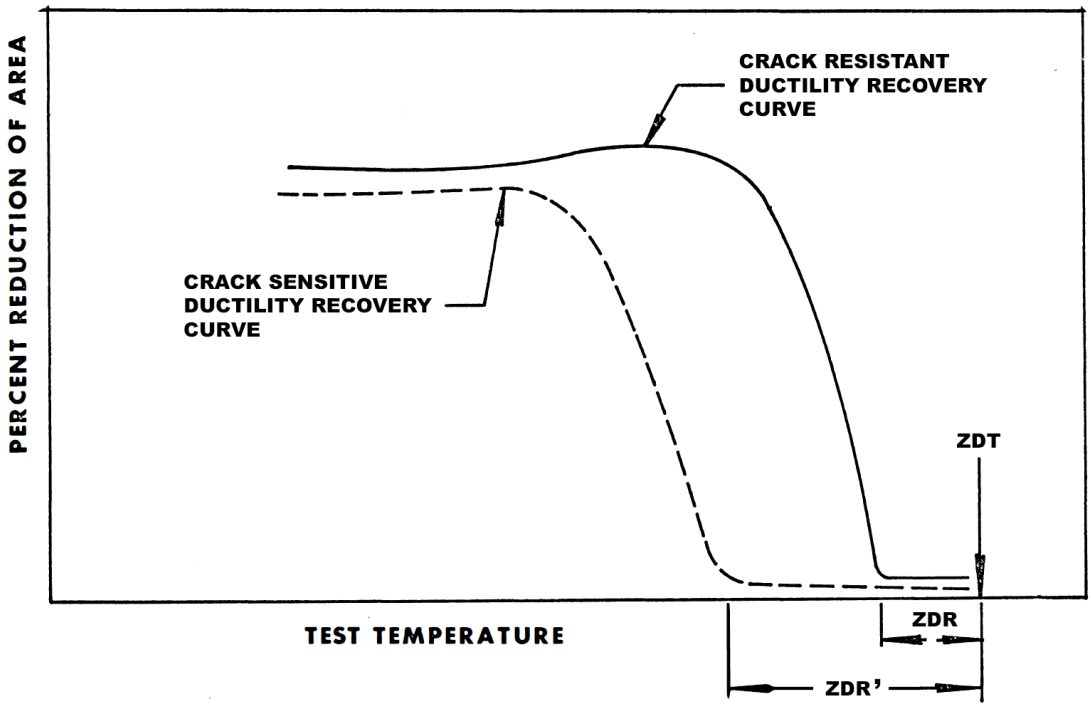

Figure 2.7: Schematic of hot ductility curves illustrating different on-cooling behaviors according to the zero ductility range (ZDR) criteria: crack-sensitive (ZDR′) and crack-resistant (ZDR). Adapted from Yeniscavich [24, Fig. 4]

Chapter 3

Materials

The 20Cr-32Ni-1Nb materials (ASTM A351 Grade CT15C) utilized in this study were provided by an industry partner and were obtained from two centrifugally-cast reducer cones removed from a hydrogen reformer outlet manifold after approximately 15 years in service (131,000 h). Typical operating conditions for these components were on the order of 857 °C (1575 °F) and 3.6 MPa (517 psi). One cone was reportedly removed in service-exposed condition ("Cone 1"); the other was removed in service-exposed condition, but reportedly had been given a solution-annealing heat treatment prior to the current investigation ("Cone 5"). The chemical compositions of the Cone 1 and Cone 5 materials as determined by optical emission spectroscopy (OES) are reported in Table 3.1. Both materials meet the chemical composition requirements for Grade CT15C in ASTM A351.

Table 3.1: Chemical compositions of 20Cr-32Ni-1Nb materials (ASTM A351 Grade CT15C [7]) utilized in the current study.

Element	Cone 1 (wt. %)	Cone 5 (wt. %)	ASTM A351-2010 Grade CT15C (wt. %)
C	0.108	0.116	0.05–0.15
Mn	1.12	1.11	0.15–1.50
P	0.008	0.009	0.03 max
S	0.007	0.007	0.03 max
Si	1.02	0.97	0.50–1.50
Ni	32.26	33.06	31.0–34.0
Cr	19.26	19.23	19.0–21.0
Mo	0.019	0.018	···
V	0.039	0.038	···
Nb	1.1	1.06	0.50–1.50
Ti	0.006	0.004	···
Co	0.027	0.023	···
Cu	0.01	0.01	···
Al	0.03	0.036	···
B	0.0003	0.0002	···
W	0.03	0.03	···
Sb	<0.001	<0.001	···
As	<0.001	<0.001	···
Sn	0.004	0.004	···
Zr	<0.001	<0.001	···
Pb	0.001	<0.001	···
Zn	0.002	0.002	···
Ta	<0.01	<0.01	···
Ca	0.0014	0.0012	···
Bi	0.0114	0.0139	···
Fe	44.77	44.12	Balance

Chapter 4

Experimental Methods

4.1 Hot Ductility Tests

Standard hot ductility samples with dimensions of 114 mm (4.5 in) [length] by 6.35 mm (0.25 in) [diameter] were extracted from the Cone 1 and Cone 5 base metals adjacent to the respective cone-to-tee welds where cracking during repair welding had been observed. A thermal cycle characteristic of shielded metal arc welding (SMAW) with 2.75 kJ mm^{-1} (70 kJ in^{-1}) energy input in 38 mm (1.5 in) stainless steel plate [39], with an initial plate temperature of 27 °C (80 °F), was utilized for the on-heating hot ductility tests. This thermal cycle was determined using the F(s,d) method [33] based on data provided by Dynamic Systems, Inc. [40]. The peak temperature of the chosen thermal cycle was 1343 °C (2450 °F), equal to the estimated solidus temperature for the CT15C alloy based on data for Incoloy 800H (CT15C is considered a "cast" version of 800H) and which would

roughly correspond to the maximum temperature experienced at the weld fusion line.

Once the on-heating hot ductility tests had been performed using the aforementioned thermal cycle and the ZDT had been determined, the thermal cycle was re-scaled so that the peak temperature was equal to the ZDT. The modified thermal cycle was subsequently used to perform the on-cooling hot ductility tests. Both the on-heating and on-cooling tests were conducted according to the parameter guidelines recommended by a detailed study [41] undertaken to establish a standardized procedure for hot ductility testing. The specific test parameters utilized in the current work are given in Table 4.1. For each test, the output of the control thermocouple was recorded, and the post-test cross-sectional area was determined and used to calculate the ductility in terms of percent reduction in area for each specimen. The collected data were used to create plots of on-heating and on-cooling ductility (% RA) as a function of test temperature.

4.2 Microstructure Characterization

Metallographic evaluations were conducted for the as-received Cone 1 and Cone 5 materials, utilizing remnants of the slices removed from the cones for machining of the hot ductility samples. Metallography was also performed on selected hot ductility samples. The hot ductility samples were sectioned longitudinally and

Table 4.1: Parameters and Conditions Used for Hot Ductility Testing, Based on Recommendations in Lundin *et al.* [41]

Parameter	Condition
Thermal Cycle	38 mm (1.5 in) stainless steel plate, SMAW process, 2.75 kJ mm^{-1} (70 kJ in^{-1}) energy input, 27 °C (80 °F) initial plate temperature
Sample	114 mm (4.5 in) length, 6.35 mm (0.25 in) diameter, 1/4-20 thread
On-Cooling Peak Temp.	Zero Ductility Temperature determined from On-Heating Curve
Crosshead Speed	50 mm s^{-1} (2 in s^{-1})
Jaw Separation	16 mm (0.625 in)
Control Thermocouple	0.25 mm (0.01 in) diameter Chromel-Alumel; Percussion Welding / Separate attachment technique, 1 mm wire spacing
Test Atmosphere	Air

mounted in castable epoxy and were subsequently ground and polished to a 0.05 µm finish. The polished samples were electrolytically etched with an aqueous 10% oxalic acid solution using a stainless steel cathode (50 mm (2 in) spacing between the sample and cathode). For the as-received base metal samples, a potential of 6 V for 3 s–5 s was used; for the hot ductility samples, it was found that a lower potential, 1.5 V for 3 s, was necessary to avoid excessive attack of certain phases near the fracture surfaces. Optical light microscopy (OLM) examination of the etched samples was performed with a Nikon MA-200 inverted metallograph equipped with a 12 megapixel digital camera for obtaining micrographs. Scanning electron microscopy (SEM) examination was conducted on selected samples using a LEO Gemini 1525 field emission SEM equipped with an Oxford Instruments

PentaFet energy dispersive x-ray spectroscopy (EDXS) system. Typically, a beam voltage of 20 kV was used for both secondary electron (SE) and back-scattered electron (BSE) imaging and for EDXS analysis.

Chapter 5

Results and Discussion

5.1 Hot Ductility Curves

The on-heating and on-cooling hot ductility curves for the Cone 1 and Cone 5 materials are presented in Figure 5.1 and Figure 5.2 respectively. In general, the on-heating ductility for both Cones increased with testing temperature, up to a ductility maximum, before dropping rapidly to zero over a short temperature range. From Figure 5.1 and Figure 5.2, it is apparent that Cone 1 and Cone 5 also showed similar trends in on-cooling behavior, in that the on-cooling ductility remains essentially zero for a definite temperature range below the ZDT before gradually increasing at lower test temperatures. Specifically for Cone 1, it is apparent from Figure 5.1 that the Cone 1 material exhibited an on-heating ZDT of 1302 °C (2375 °F) and an on-cooling ductility recovery temperature (DRT) of 1260 °C (2300 °F), resulting in a ZDR of 24 C° (75 F°). Figure 5.2 shows that the

Cone 5 material also exhibited an on-heating ZDT of 1302 °C (2375 °F), DRT of 1260 °C (2300 °F), and ZDR of 24 C° (75 F°). These characteristics of the hot ductility curves for both materials are summarized in Table 5.1.

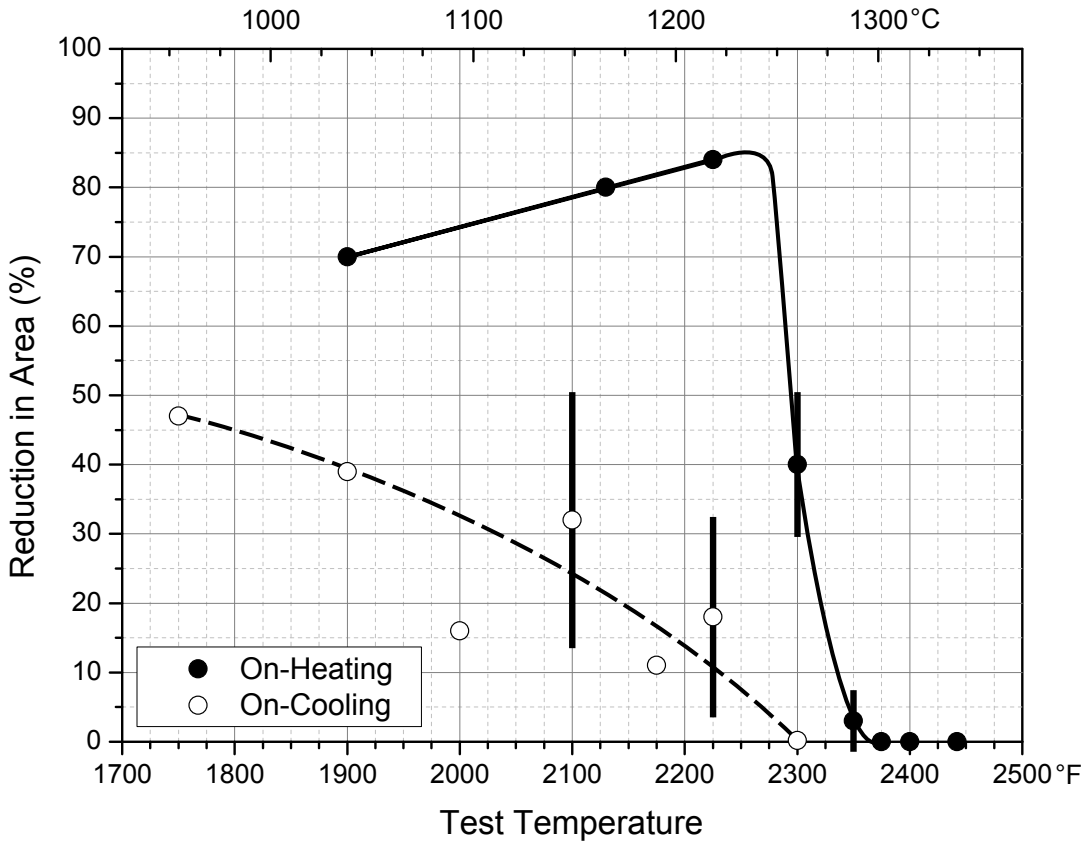

Figure 5.1: Hot ductility behavior of CT15C Cone 1 base metal. Bars indicate range of % RA values at indicated test temperature. On-heating curve exhibits Class H1 behavior with ZDT = 1302 °C (2375 °F). On-cooling curve (from peak temperature equal to ZDT) exhibits Class C3 behavior. DRR(1218 °C (2225 °F)) = 21%. Hot ductility test parameters are given in Table 4.1.

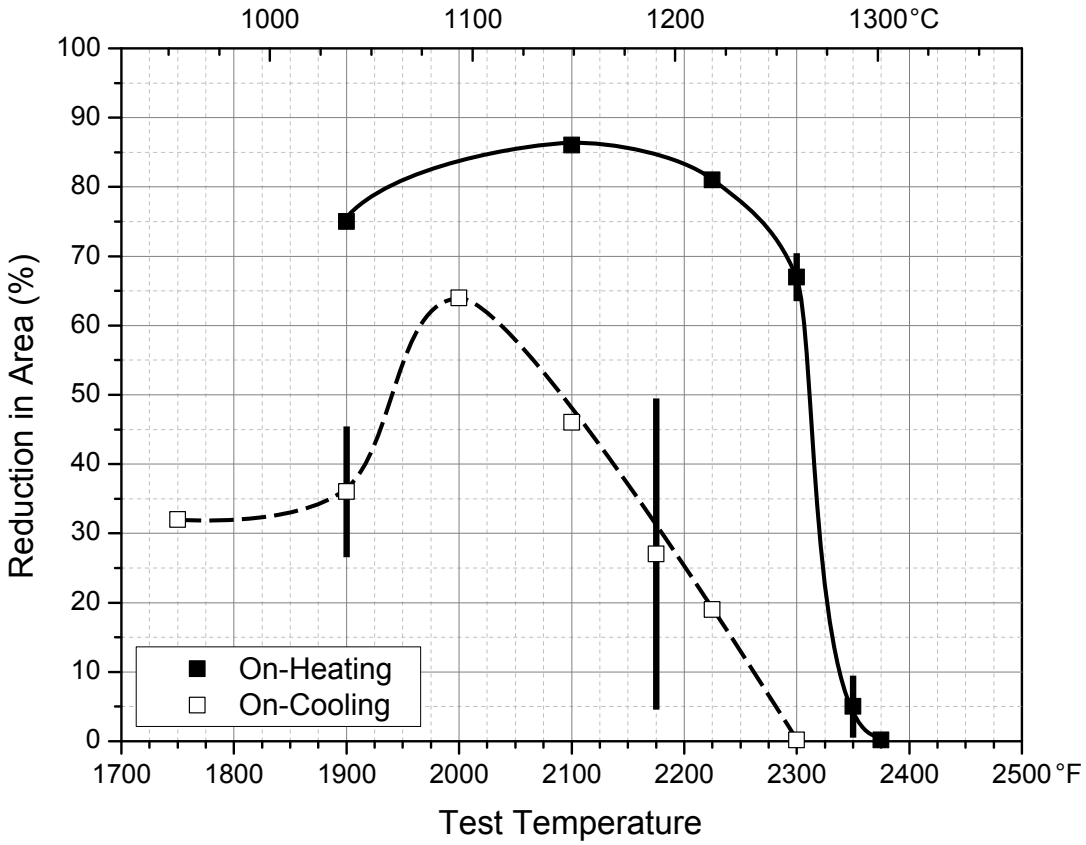

Figure 5.2: Hot ductility behavior of CT15C Cone 5 base metal. Bars indicate range of % RA values at indicated test temperature. On-heating curve exhibits Class H1 behavior with ZDT = 1302 °C (2375 °F). On-cooling curve (from peak temperature equal to ZDT) exhibits Class C3 behavior. DRR(1218 °C (2225 °F)) = 23%. Hot ductility test parameters are given in Table 4.1.

Table 5.1: Summary of hot ductility characteristics for Cone 1 and Cone 5 materials, as determined from the curves in Figure 5.1 and Figure 5.2.

Material ID and Condition	**ZDT**	**DRT**	**ZDR (ZDT-DRT)**
Cone 1	1302 °C (2375 °F)	1260 °C (2300 °F)	24 C° (75 F°)
Cone 5	1302 °C (2375 °F)	1260 °C (2300 °F)	24 C° (75 F°)

As can be seen from Figure 5.1 and Figure 5.2, the on-heating hot ductility curves for both Cone materials appear similar, with similar reduction in area (% RA) values at each test temperature, except in the vicinity of 1260 °C (2300 °F). At this temperature, Cone 1 exhibits a more rapid loss in ductility than Cone 5. It should be noted that the on-heating ZDT of both materials, determined to be 1302 °C (2375 °F), is well below the bulk solidus temperature for 20Cr-32Ni-1Nb which is on the order of 1393 °C (2540 °F) [21]. Based on the Nippes evaluation criteria [38] described previously, examination of the shape of the on-heating ductility curves in Figure 5.1 and Figure 5.2 shows that both Cones exhibit Class H1 on-heating hot ductility behavior rather than Class H2 behavior. This observation regarding the Cone 1 and Cone 5 materials is indeterminate on its own, as Nippes *et al.* [38] observed in some cases that two materials which both showed H1 on-heating behavior were later found to exhibit either crack-sensitive or crack-insensitive characteristics when tested on-cooling.

Considering the shapes of the on-cooling ductility curves for the Cone 1 and Cone 5 materials after exposure to a peak temperature corresponding to the on-heating ZDT (1302 °C (2375 °F)), as shown in Figure 5.1 and Figure 5.2, it is apparent that both Cone materials exhibit Class C3 on-cooling behavior when exposed to the ZDT, based on the Nippes criteria (Figure 2.5). This category of on-cooling behavior is associated with the greatest degree of hot cracking susceptibility as established by Nippes *et al.* [38]. While in general both materials exhibit Class C3 behavior, it appears from Figure 5.1 and Figure 5.2 that Cone 5

shows a slightly better qualitative recovery of on-cooling ductility than Cone 1. As shown in Figure 5.2, the on-cooling ductility for Cone 5 recovers to higher values than for Cone 1, particularly at 1149 °C (2100 °F) and 1093 °C (2000 °F). However, when considering the apparent difference, it should be noted that both Cones are cast components with a large dendrite size, and it was observed in early work on hot ductility by Nippes *et al.* [38] that castings typically showed wider variation in ductility values at a given test temperature than was observed for wrought material. The 20Cr-32Ni-1Nb cast material used in both Cones is no different in this regard, for example as evidenced by the variation at 1149 °C (2100 °F) on-cooling for Cone 1 and at 1191 °C (2175 °F) on-cooling for Cone 5. Due to the reality of variations in ductility values, it is recommended practice (Lundin *et al.* [41]) to run a minimum of two hot ductility tests at each temperature, with some studies (Nippes *et al.* [38]) running up to four tests per temperature for cast materials. Unfortunately, the number of samples available in the current study was not sufficient to permit duplicate tests at all test temperatures, although duplicates were performed wherever possible, including at the ZDT. If sufficient samples had been available for duplicate tests at all temperatures, it is possible that the average % RA at certain test temperatures (e.g. 1093 °C (2000 °F) on-cooling and 1149 °C (2100 °F) on-cooling) would be closer in magnitude between Cone 1 and Cone 5. Taking these considerations into account, it is likely that Cone 1 and Cone 5 are more similar in on-cooling behavior than would be suggested by a casual inspection of the curves in Figure 5.1 and Figure 5.2.

To quantify the severity of the on-cooling ductility loss exhibited by both materials, the ductility recovery rate (DRR) was determined for both Cone 1 (Figure 5.1) and Cone 5 (Figure 5.2) at a test temperature of 1218 °C (2225 °F) since this corresponds most closely with the observed rapid-ductility-decrease temperature (on-heating) for both Cones. The DRR at 1218 °C (2225 °F) was similarly low for both Cone materials: 21% for Cone 1 and 23% for Cone 5. Additionally, both Cones exhibited a region of zero on-cooling ductility (ZDR) after exposure to the on-heating ZDT; for both Cone 1 and Cone 5, the ZDR exists over a 24 C° (75 F°) interval between 1260 °C–1301 °C (2300 °F–2375 °F). Considered together, the occurrence of Class C3 cooling behavior, the relatively low DRR values, and the presence of a ZDR all indicate that the Cone 1 and Cone 5 materials are both susceptible to HAZ liquation cracking when exposed to peak temperatures typically experienced during a welding thermal cycle. Compared to other heat-resistant alloys, the hot ductility behavior of 20Cr-32Ni-Nb as revealed in Figures 5.1 and 5.2 is similar to the behavior of "crack sensitive" Alloy 800H material (e.g. as shown in Figure 5.3) as investigated by Qiao [42] using hot ductility and Varestraint testing. For comparison, Qiao also evaluated the hot ductility of standard-chemistry 316 stainless steel which showed substantially better ductility recovery, with a minimal ZDR and Class C1/C2 on-cooling recovery as shown in Figure 5.4.

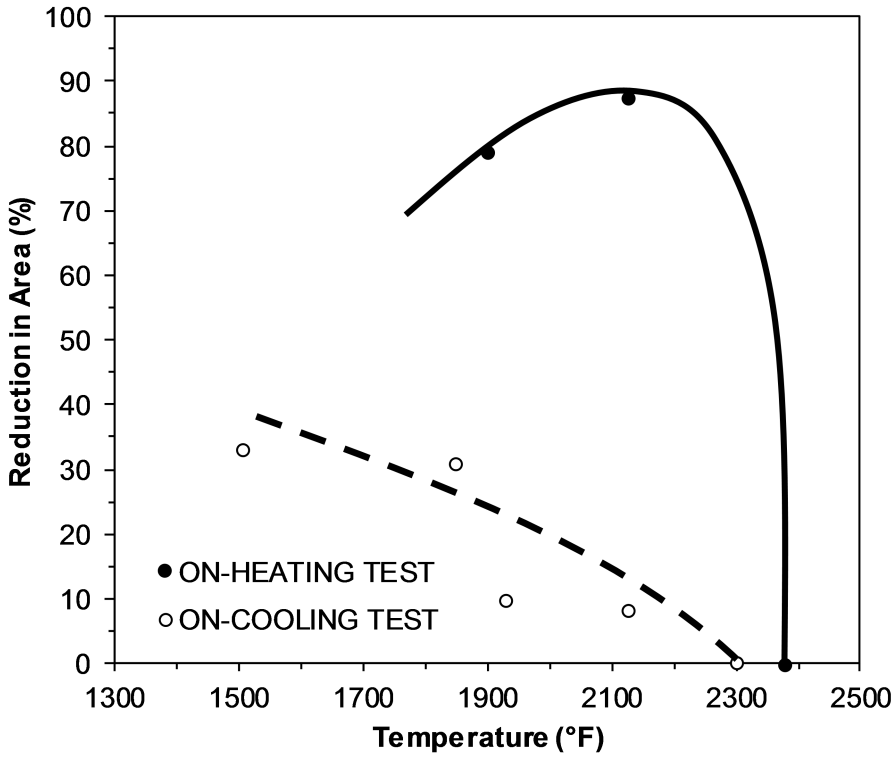

Figure 5.3: Hot ductility behavior of wrought modified 800H material exhibiting poor ductility recovery and classified as being sensitive to HAZ liquation cracking based on hot ductility and Varestraint testing. Adapted from Qiao [42].

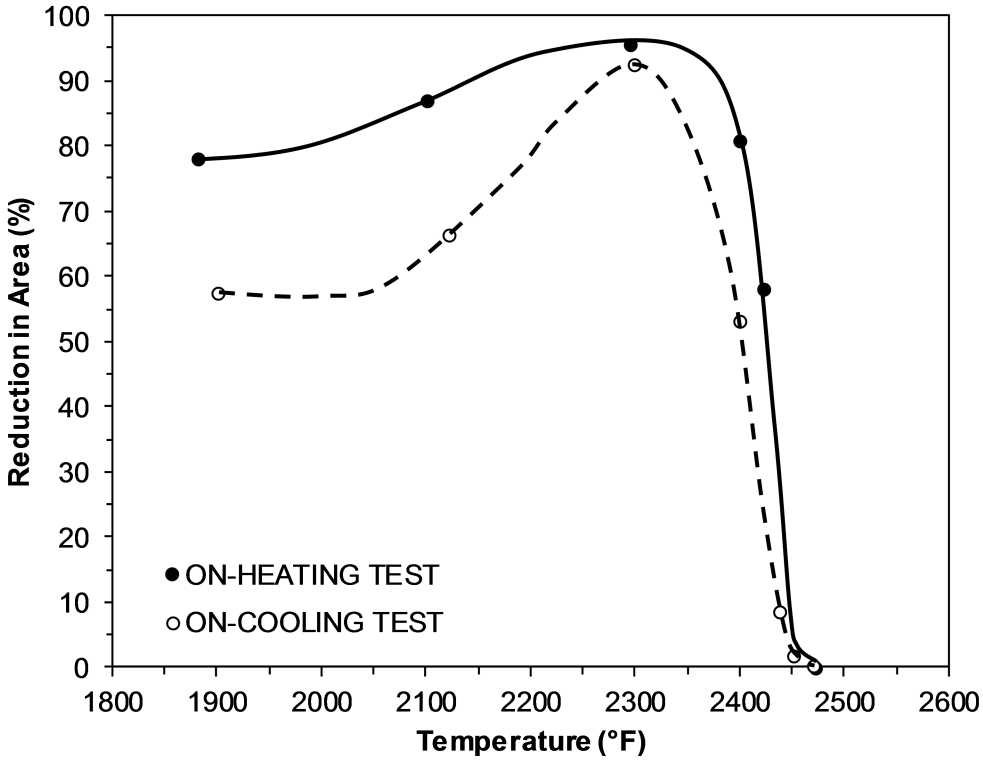

Figure 5.4: Hot ductility behavior of 316 stainless steel exhibiting excellent ductility recovery with correspondingly low susceptibility to HAZ liquation cracking. Adapted from Qiao [42].

5.2 Microstructural Characterization

5.2.1 Characterization of As-Received Base Metals

The typical as-received microstructures for the Cone 1 and Cone 5 materials, respectively, are shown in the optical micrographs in Figure 5.5 and Figure 5.6. Both Cone materials exhibited a cast, dendritic structure with a large dendrite size. The 500X magnification micrographs in Figure 5.5b and Figure 5.6b show the presence of abundant fine intradendritic precipitates in the austenite matrix in addition to the larger phases along the interdendritic boundaries. The as-received Cone 1 and Cone 5 base metals were also examined in the SEM to perform EDXS analyses of some of the constituents. SEM micrographs and EDXS results for typical Cone 1 and Cone 5 microstructures are presented in Figures 5.7 and 5.8 and Figures 5.9 and 5.10, respectively. For Cone 1 material, Figure 5.7 shows both coarse interdendritic phases (e.g. "A" in Figure 5.7b) and clusters of finer precipitates ("B" in Figure 5.7b). The EDXS results in Figure 5.8, corresponding to points "A" and "B" in Figure 5.7b, show a high amount of niobium, indicating that both regions consist of niobium carbides (NbC). It should be noted that in Figure 5.8 (and all subsequent EDXS determinations), carbon has been excluded from the quantitative results because it is difficult to accurately assess carbon with EDXS. These interdendritic NbC particles are apparent in the optical micrographs in Figures 5.5 and 5.6 (e.g. as the larger phases appearing as "salmon"-colored, which is their natural appearance when viewed with OLM). The chromium, iron,

and nickel contents reported for point "B" are considered to arise from beam interaction with the surrounding matrix, due to the small size of the analyzed particles. Similarly for the Cone 5 material, Figure 5.9 shows coarse interdendritic phases ("A" in Figure 5.9b) with finer phases present at the periphery (area "B" in Figure 5.9b). Both "A" and "B" in Figure 5.9b contain a high amount of niobium as shown in Figure 5.10, corresponding to NbC. The compositions of the very fine (« 1 µm) intradendritic precipitates, visible in both Cone 1 and Cone 5 in Figure 5.7a and Figure 5.9a respectively, were not determined because these precipitates are too small to be analyzed with EDXS.

It should be noted that in service-exposed 20Cr-32Ni-Nb material, the formation of a secondary phase rich in nickel, niobium, and silicon (Ni-Nb silicide, or G-phase) around the NbC carbides often occurs as reported by a number of authors [21, 22, 43, 44]. The formation of Cr-rich $M_{23}C_6$ carbides along the interdendritic boundaries has also been reported after service exposure [43, 44]. However, the presence of Cr-rich $M_{23}C_6$ carbides or Ni-Nb-Si-rich phases around the NbC carbides was not observed in either the as-received Cone 1 or Cone 5 materials despite the fact that they were reported to be in service-exposed condition, with 15 y of exposure at 857 °C (1575 °F). Hoffman [21] observed differences in the extent of Ni-Nb-Si-rich phase formation (which he identified as G-phase) between statically cast tees and centrifugally cast cones with different compositions, with the cone material having a lesser (unspecified) extent of silicide formation. Compared to the service conditions and materials reported by other

workers [21, 22, 43, 44], in some cases the Cone 1 and Cone 5 materials (this study) reportedly have longer service exposure time or higher service temperature. In a 25Cr-32Ni-2Nb alloy, higher temperatures (982 °C (1800 °F)) were associated with reduced stability of G-phase [17]. However, this temperature is well above the reported service temperature of the two materials examined in this study, making it unlikely that the reported service temperature of 857 °C (1575 °F) for Cone 1 and Cone 5 is responsible for the disparity between observation of G-phase as reported in the literature and the lack of G-phase in the current materials. The most likely explanation for the apparent absence of Ni-Nb silicide phases in the as-received Cone 1 and Cone 5 materials is that the materials were solution annealed after removal from service, as this type of heat treatment at temperatures in the range of 1149 °C (2100 °F) has been observed to dissolve the Ni-Nb silicides [21, 45].

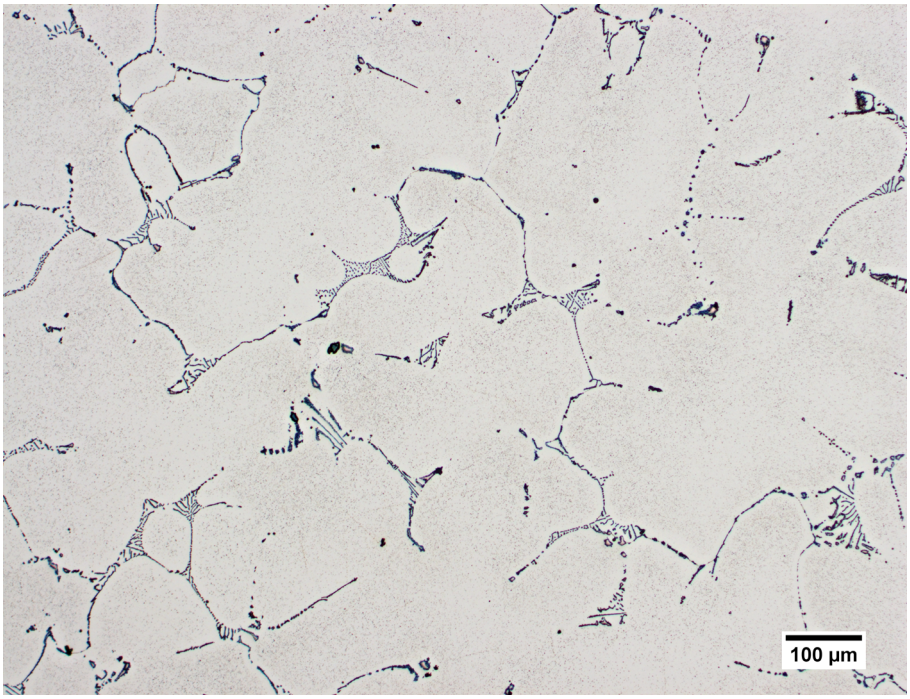

(a) 100X

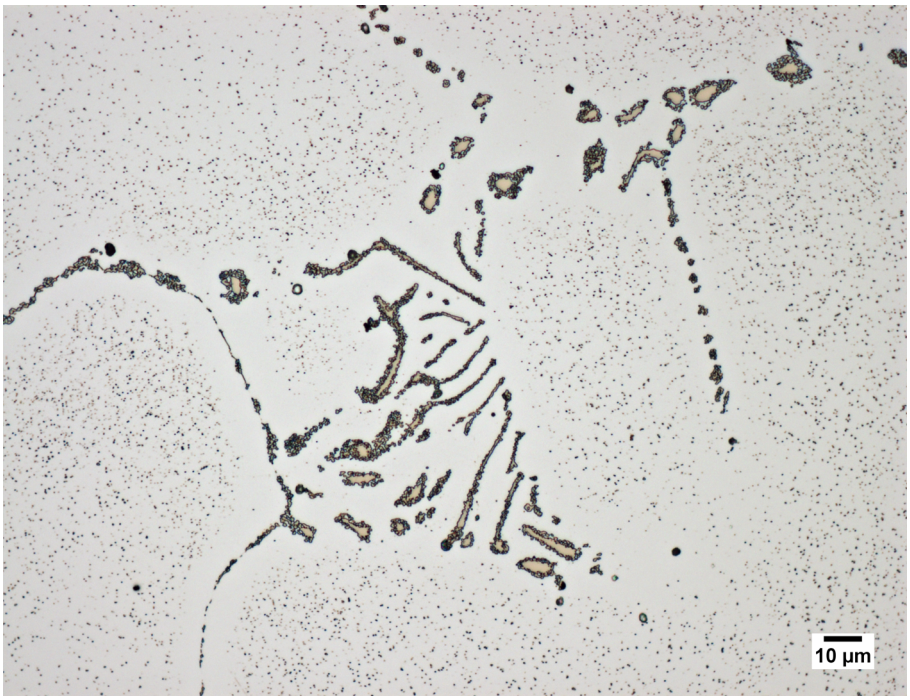

(b) 500X

Figure 5.5: Optical micrographs showing the typical as-received microstructure of Cone 1 material utilized for hot ductility testing. Etch: electrolytic 10% oxalic acid.

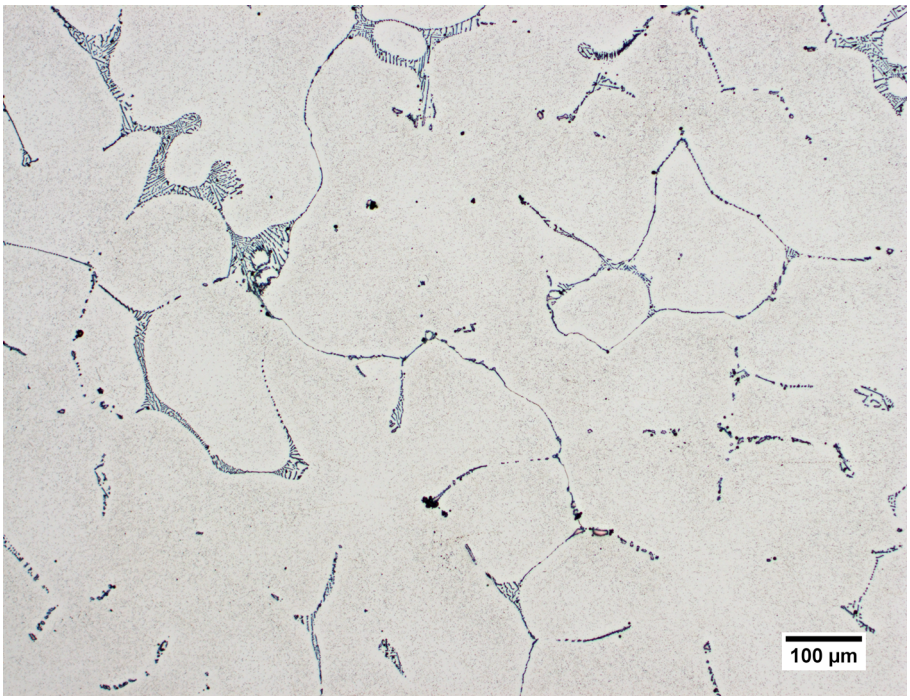

(a) 100X

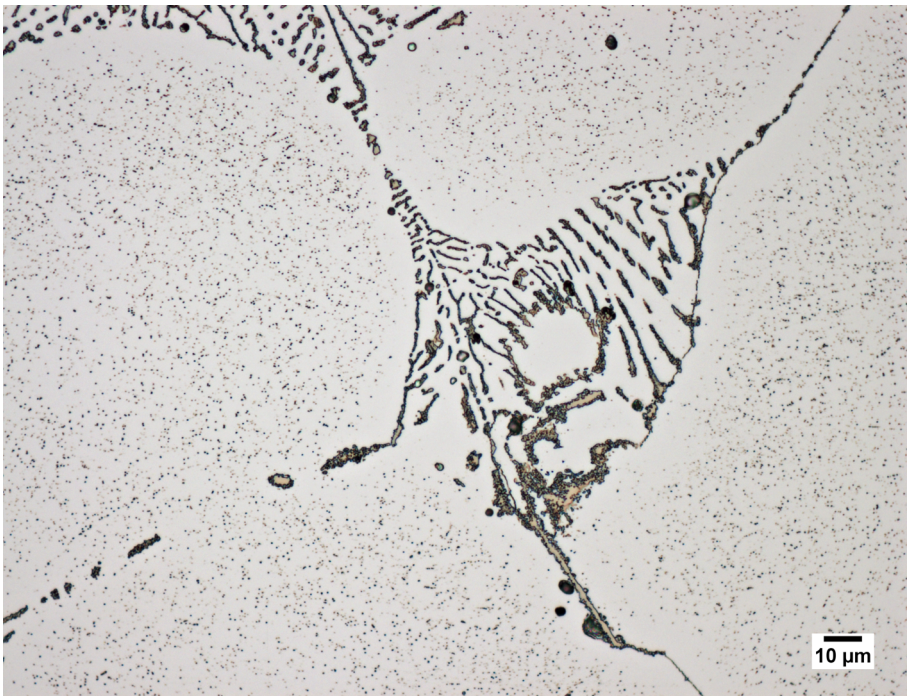

(b) 500X

Figure 5.6: Optical micrographs showing the typical as-received microstructure of Cone 5 material utilized for hot ductility testing. Etch: electrolytic 10% oxalic acid.

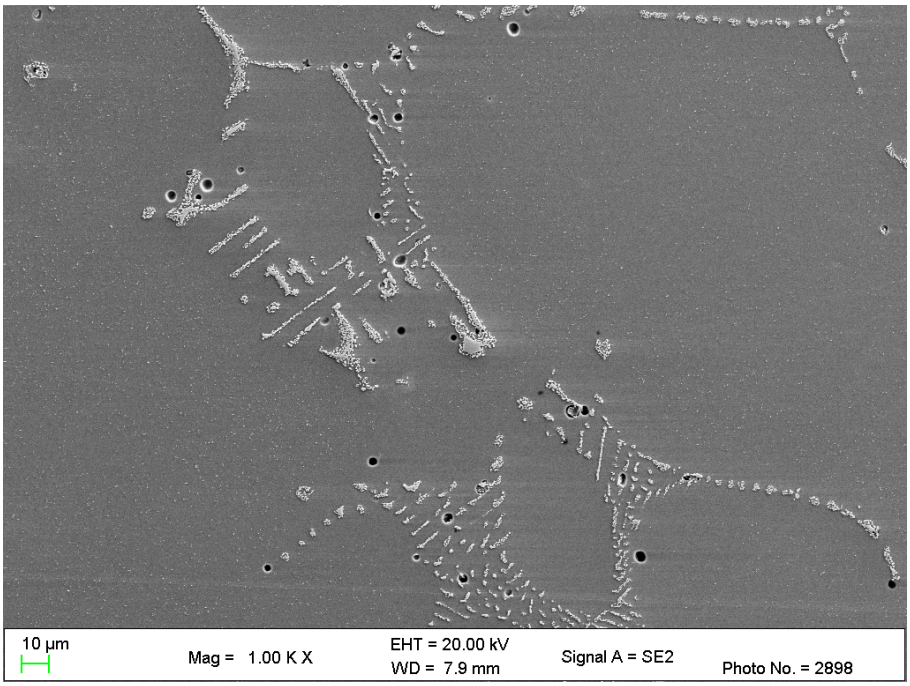

(a) 1000X

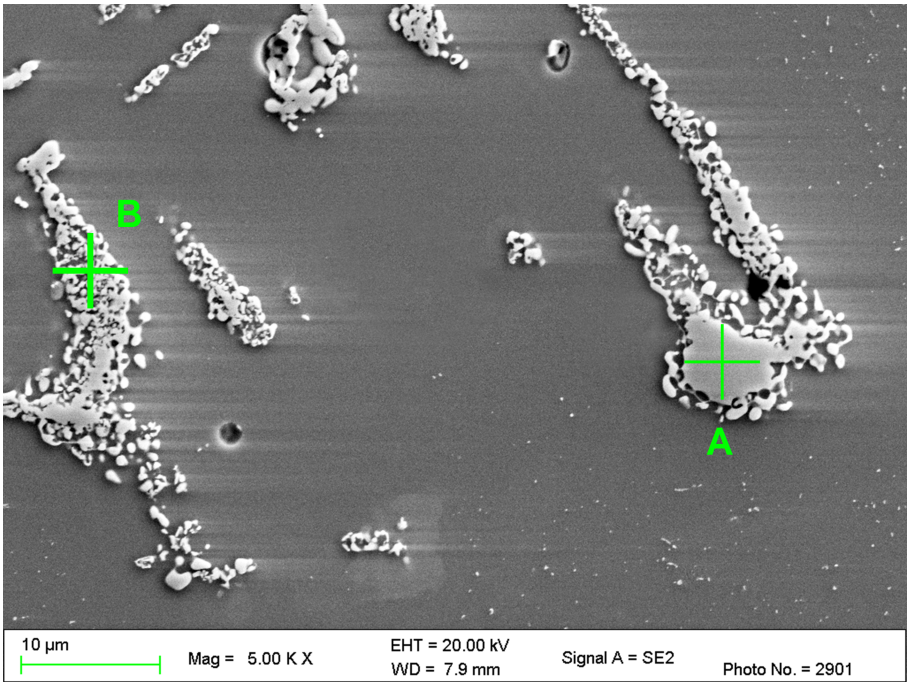

(b) 5000X

Figure 5.7: SEM micrographs showing typical intradendritic and interdendritic phases present in Cone 1 material utilized for hot ductility testing. EDXS spot analysis results for labeled locations "A" and "B" are given in Figure 5.8. Etch: electrolytic 10% oxalic acid.

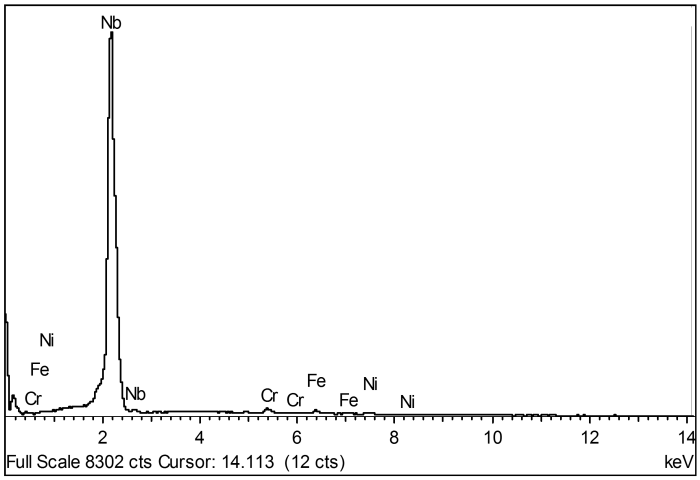

Element	Analysis (wt. %)	Analysis (at. %)
Nb	96	94
Cr	1	2
Fe	1	2
Ni	1	2

(a) Spot Analysis "A"

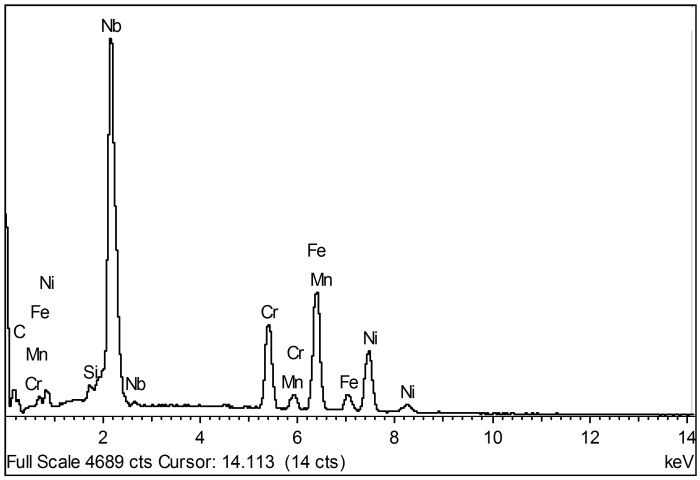

Element	Analysis (wt. %)	Analysis (at. %)
Nb	46	34
Cr	12	16
Fe	23	28
Ni	17	20
Si	0.7	1.8
Mn	0.9	1

(b) Spot Analysis "B"

Figure 5.8: EDXS spot analysis results for locations "A" and "B" identified in Figure 5.7b for as-received Cone 1 material.

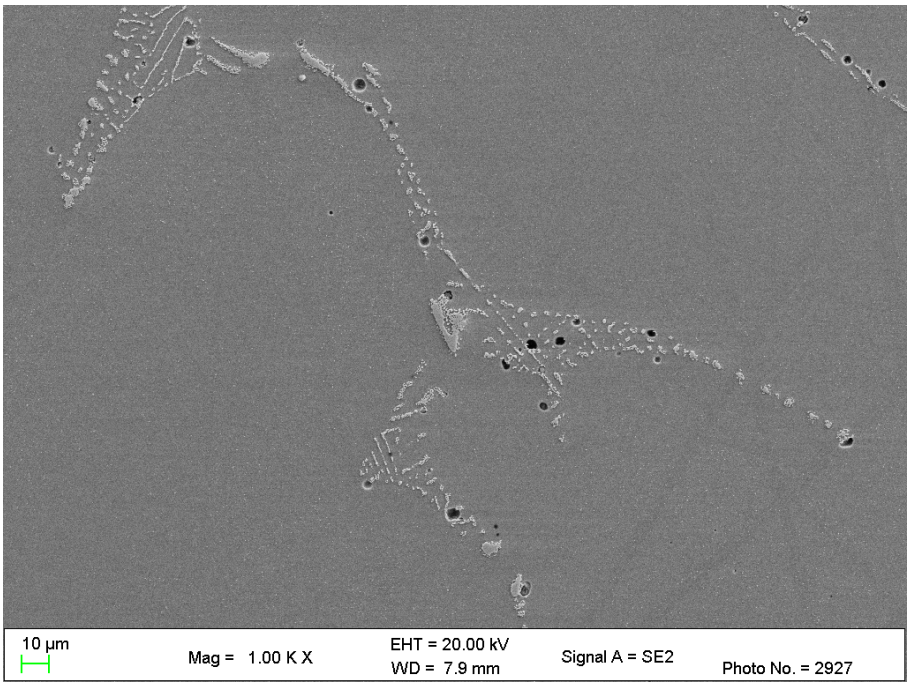

(a) 1000X

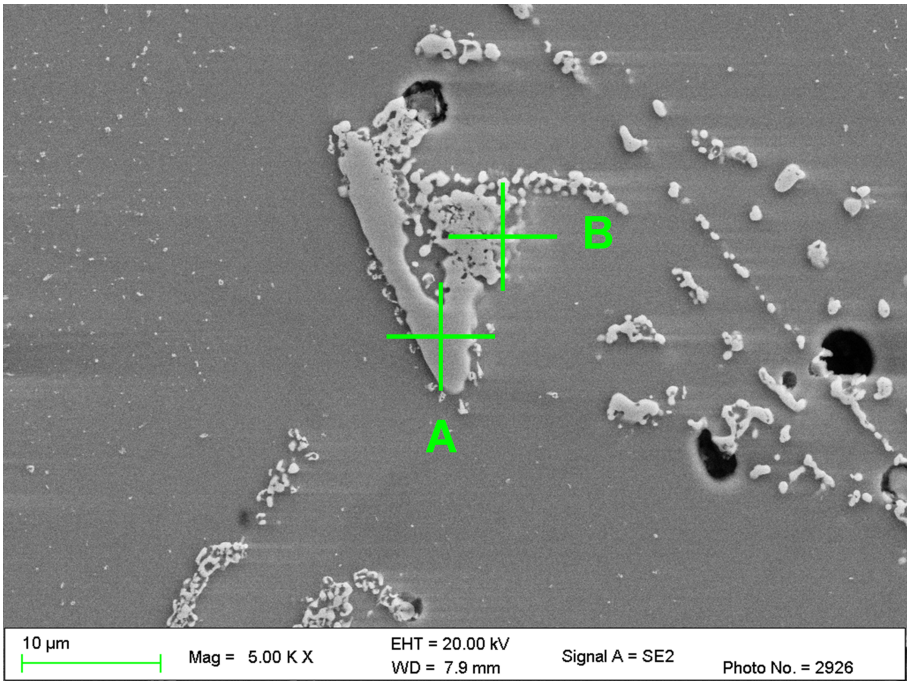

(b) 5000X

Figure 5.9: SEM micrographs showing typical intradendritic and interdendritic phases present in Cone 5 material utilized for hot ductility testing. EDXS analyses for labeled points "A" and "B" are given in Figure 5.10. Etch: electrolytic 10% oxalic acid.

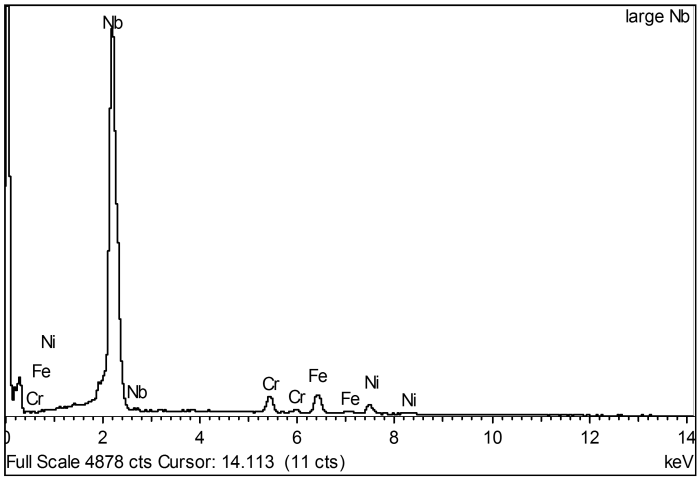

Element	Analysis (wt. %)	Analysis (at. %)
Nb	84	76
Cr	4.5	7
Fe	7	11
Ni	4.5	6

(a) Spot Analysis "A"

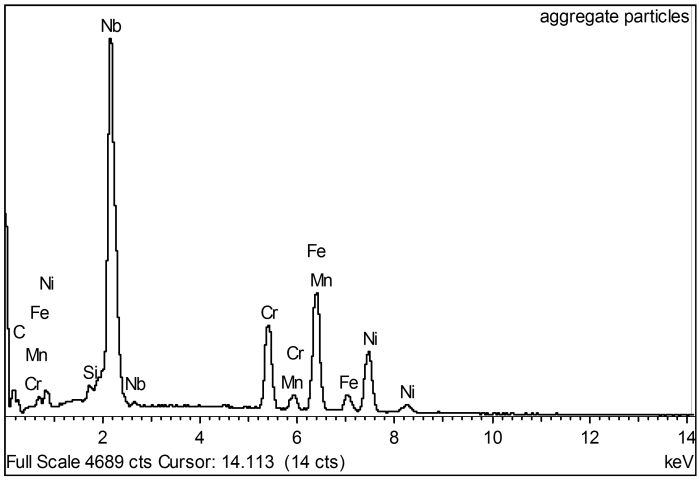

Element	Analysis (wt. %)	Analysis (at. %)
Nb	72	60
Cr	7	10
Fe	13	18
Ni	9	11

(b) Spot Analysis "B"

Figure 5.10: EDXS spot analysis results for locations "A" and "B" identified in Figure 5.9b for as-received Cone 5 material.

5.2.2 Characterization of On-Heating Hot Ductility Tests

Cone 1 On-Heating

Figure 5.11 shows a region adjacent to the fracture surface of the Cone 1 On-Heating 1302 °C (2375 °F) (C1 OH-2375) hot ductility sample. The C1 OH-2375 sample corresponds to the ZDT for Cone 1 and significant cracking is evident near the surface with the crack paths following the interdendritic boundaries. Note that in Figure 5.11, the tensile loading direction for the hot ductility test is in the vertical direction, so the crack paths are oriented perpendicular to the loading direction. It is also apparent that compared to the as-received Cone 1 microstructure (Figure 5.5), dissolution of some of the fine intradendritic precipitates has occurred due to the high temperature of the simulated thermal cycle of the hot ductility test.

The tip of the crack visible in Figure 5.11a is shown at higher magnification in Figure 5.11b, which shows evidence of liquation (where liquid was present) along the crack faces, as well as around the interdendritic boundary and associated phases ahead of the crack. The liquated regions (where localized melting occurred during the simulated thermal cycle) are denoted by arrows in Figure 5.11b and are visible as slightly brighter regions which stand faintly in relief. The evidence of prior liquid along the interdendritic boundaries (i.e. liquated boundaries) correlates with the observed zero ductility behavior observed at this temperature. As the peak temperature of the simulated thermal cycle increases to the point where the first liquid (which cannot support strain) is formed along the boundaries,

the ductility will drop to zero. Larger liquated regions are also apparent at other locations near the fracture surface in the C1 OH-2375 sample, as shown in Figure 5.12. However, in general, evidence of liquation is only intermittently present along the fracture profile of the sample shown in Figure 5.11a. The liquated region from Figure 5.12 is shown at higher magnification in the SEM micrograph in Figure 5.13 along with spot EDXS results for a location in the liquated region. It is apparent that the prior liquid, surrounding the interdendritic phases along a boundary, was not enriched in Ni or Si which is in agreement with the results for the as-received Cone 1 base metal which did not find evidence of Ni-Nb-Si-rich phases surrounding the eutectic NbC; however, a small amount Nb was detected in the prior liquid region.

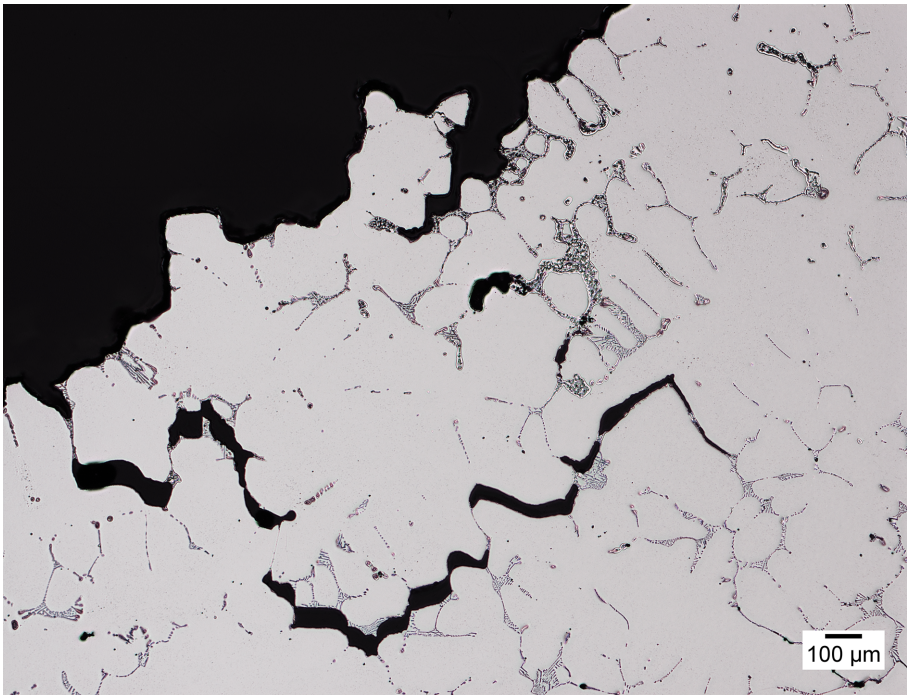

(a) 50X

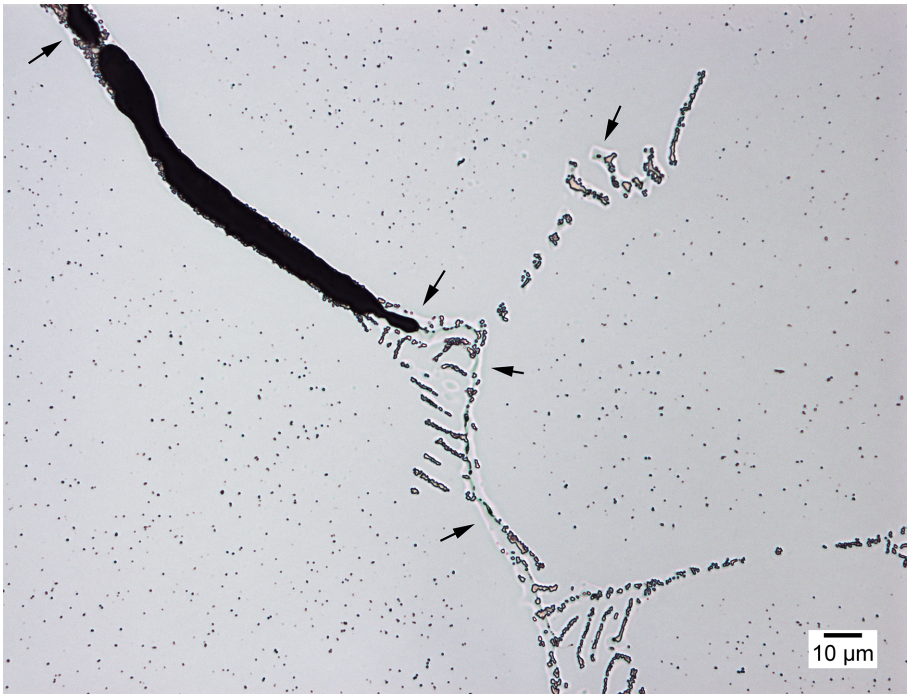

(b) 500X

Figure 5.11: Optical micrographs showing the region adjacent to the fracture surface in the Cone 1 On-Heating 1302 °C (2375 °F) hot ductility sample. Evidence of liquation (where melting occurred during the simulated thermal cycle) is denoted by arrows. Etch: electrolytic 10% oxalic acid.

(a) 100X

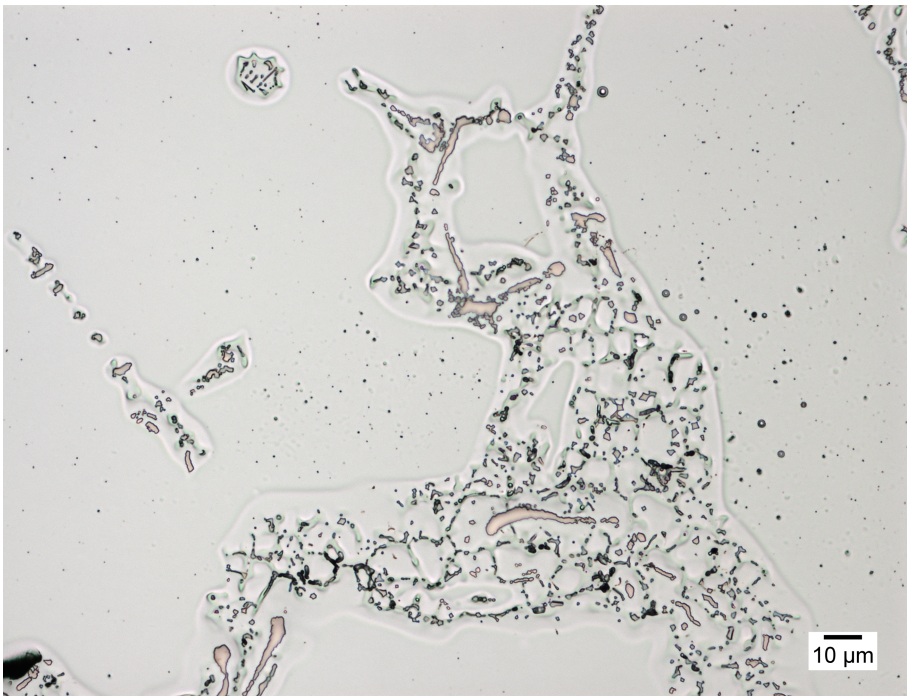

(b) 500X

Figure 5.12: Optical micrographs showing liquation around interdendritic phases adjacent to the fracture surface in the Cone 1 On-Heating 1302 °C (2375 °F) hot ductility sample. Etch: electrolytic 10% oxalic acid.

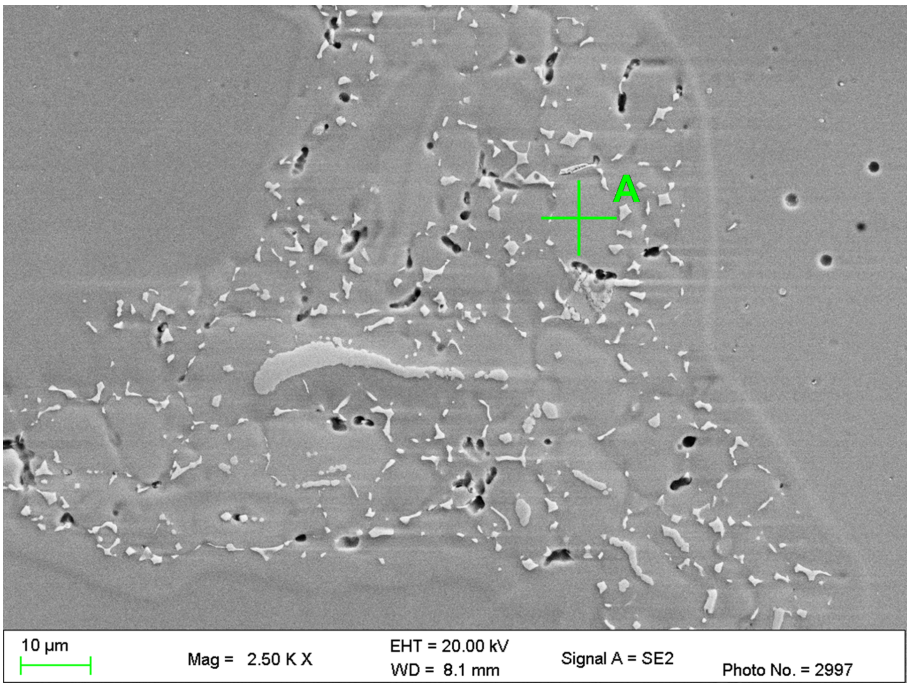

(a) SEM micrograph of liquated region

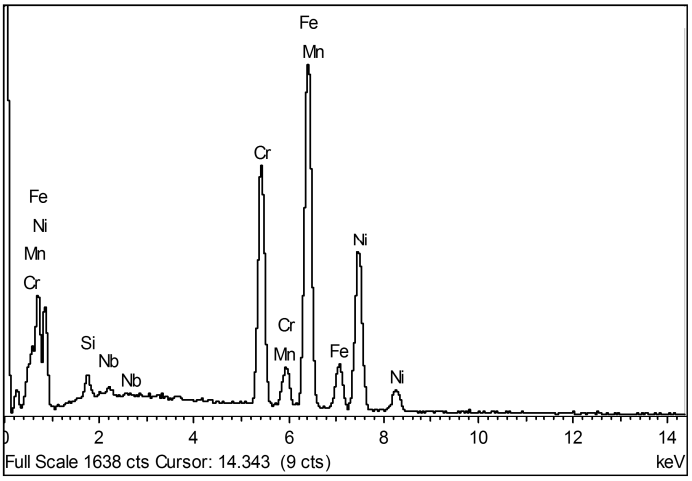

Element	Analysis (wt. %)	Analysis (at. %)
Cr	20	22
Ni	32	30
Fe	45	44
Mn	1	1
Si	1	2
Nb	0.6	0.3

(b) Spot EDXS results for point "A"

Figure 5.13: SEM micrograph showing liquation around interdendritic phases adjacent to the fracture surface in the Cone 1 On-Heating 1302 °C (2375 °F) hot ductility sample with spot EDXS results for indicated point "A" within the liquated region. Etch: electrolytic 10% oxalic acid.

Cone 5 On-Heating

Figure 5.14 shows a region at the fracture surface of the Cone 5 On-Heating 1302 °C (2375 °F) (C5 OH-2375) hot ductility sample which corresponds to the ZDT of Cone 5. As with Cone 1, cracking is evident along the interdendritic boundaries and a majority of the intradendritic precipitates have dissolved due to the high temperature exposure. The crack tip is shown in Figure 5.15 and two separate regions at the tip of the crack shown in Figure 5.15 are shown at higher magnification in Figure 5.16. It is apparent that liquated regions (where liquid was formed during the simulated thermal cycle) exist along a portion of the crack faces and around some of the interdendritic phases ahead of the crack (see arrows in Figure 5.16a). However, significant evidence of prior liquid is not apparent at the extreme tip portion where the crack is quite narrow (Figure 5.16b), indicating that minimal to no liquid was formed at this location during the simulated thermal cycle. Similarly to Cone 1, liquated regions are visible at other locations adjacent to the fracture surface away from apparent cracks, as shown in Figure 5.17. Again, the liquated regions are not present continuously along the fracture profile, indicating a lesser extent of prior liquid formation (as compared to the on-cooling tests which will be discussed later). Overall, both Cone 1 and Cone 5 showed similar microstructures for the on-heating hot ductility tests.

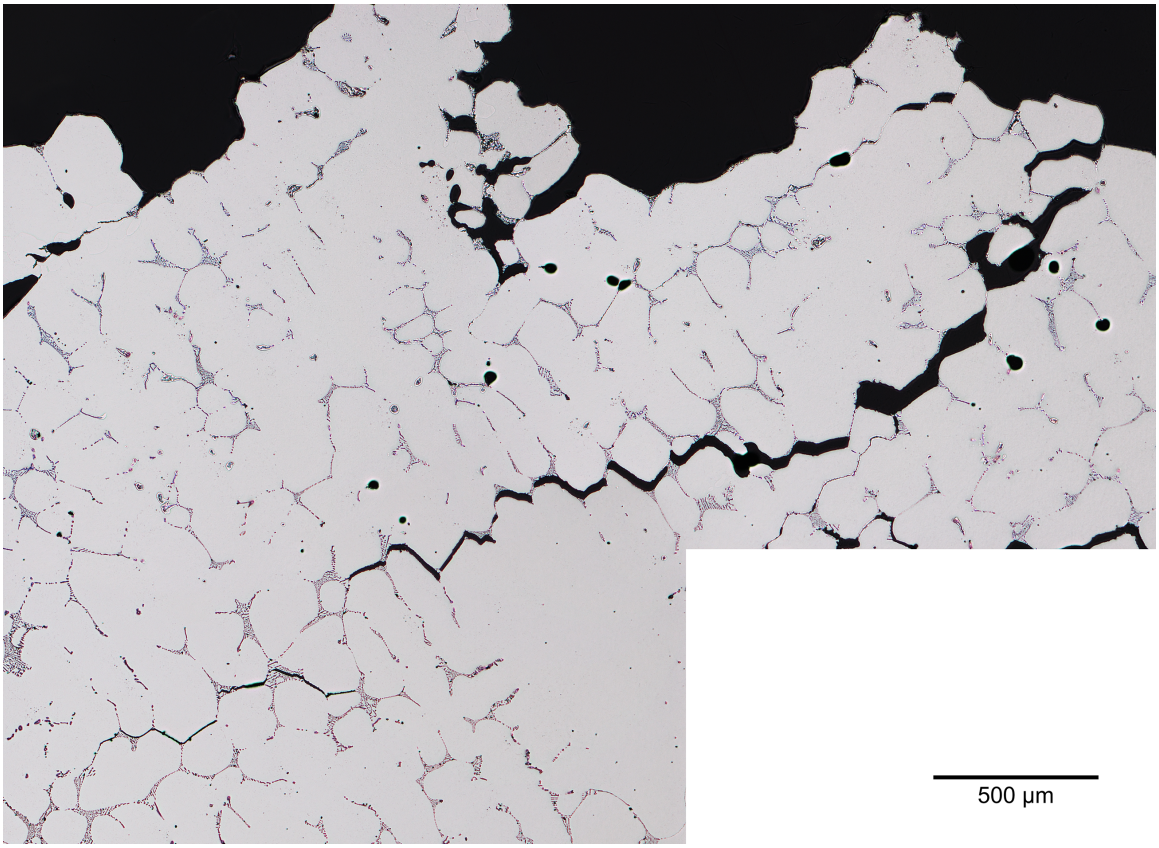

Figure 5.14: Optical micrograph showing cracking and liquation in a region adjacent to the fracture surface in the Cone 5 On-Heating 1302 °C (2375 °F) hot ductility sample. The crack tip region is shown in Figure 5.15. Etch: electrolytic 10% oxalic acid.

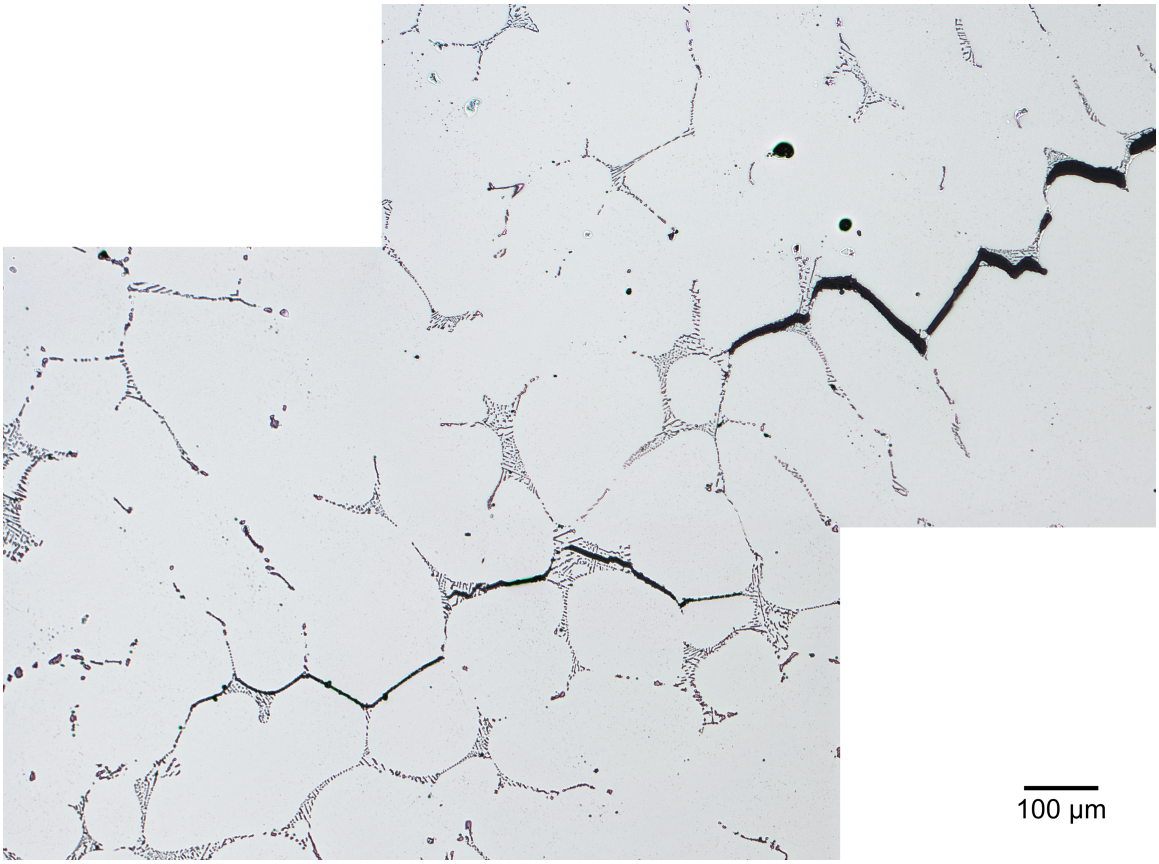

Figure 5.15: Optical micrograph of the tip of the crack visible in Figure 5.14 for the Cone 5 On-Heating 1302 °C (2375 °F) hot ductility sample. The crack tip region is shown at higher magnification in Figure 5.16. Etch: electrolytic 10% oxalic acid.

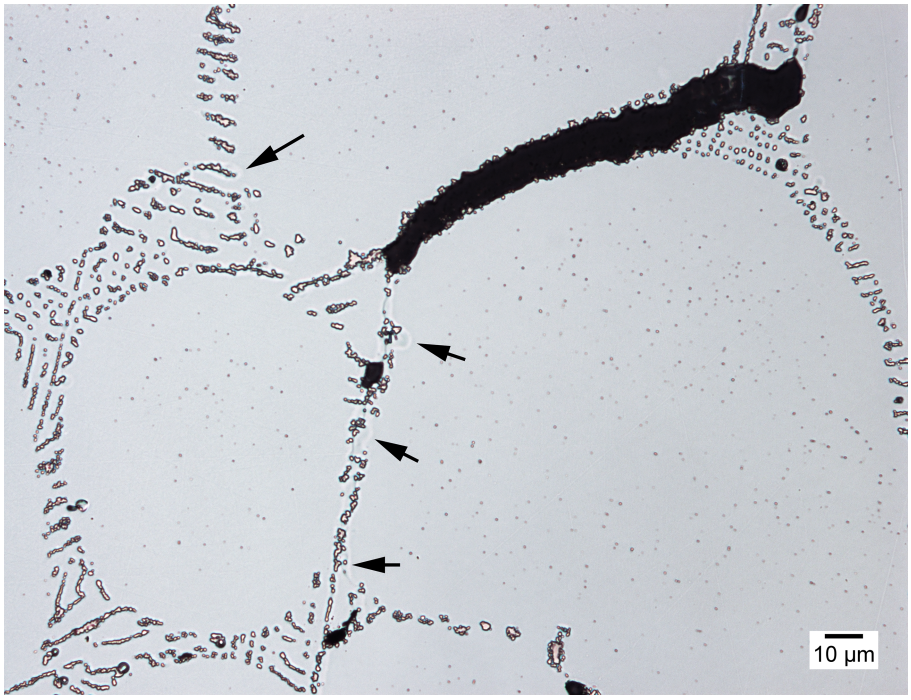

(a) Wider region near crack tip

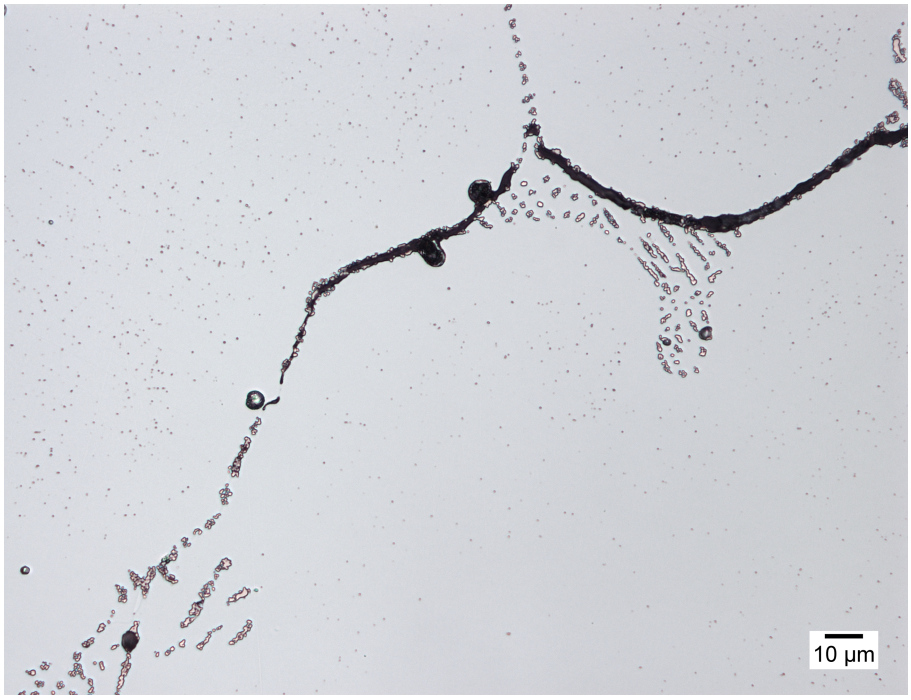

(b) Narrower region at crack tip

Figure 5.16: Optical micrographs showing wide and narrow regions at the tip of the crack visible in Figure 5.15 for the Cone 5 On-Heating 1302 °C (2375 °F) hot ductility sample. Liquation around the interdendritic phases and on the crack faces is evident in (a), as indicated by arrows, but not in (b). Etch: electrolytic 10% oxalic acid.

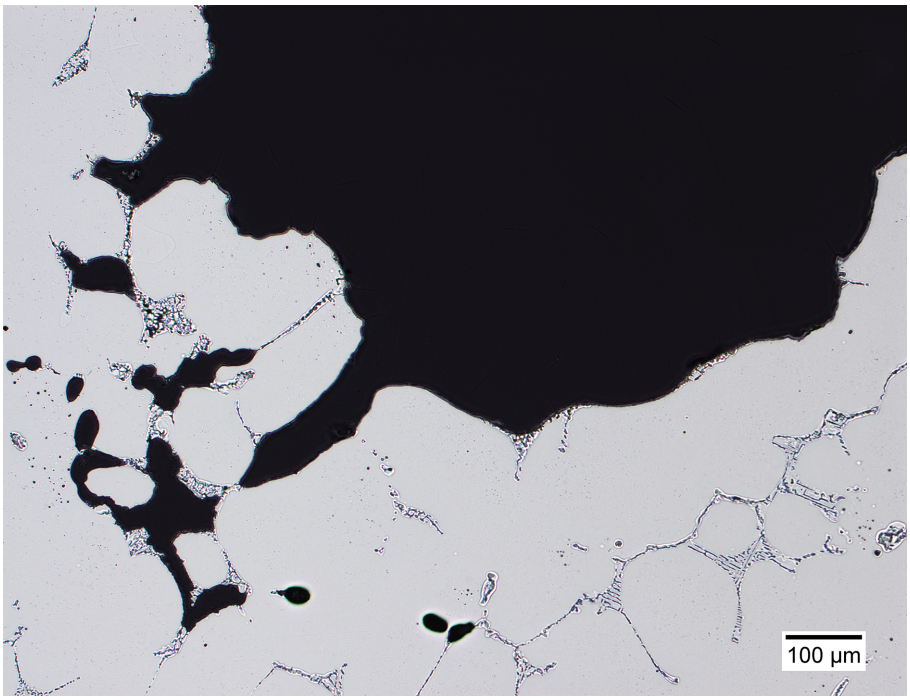

(a) 100X

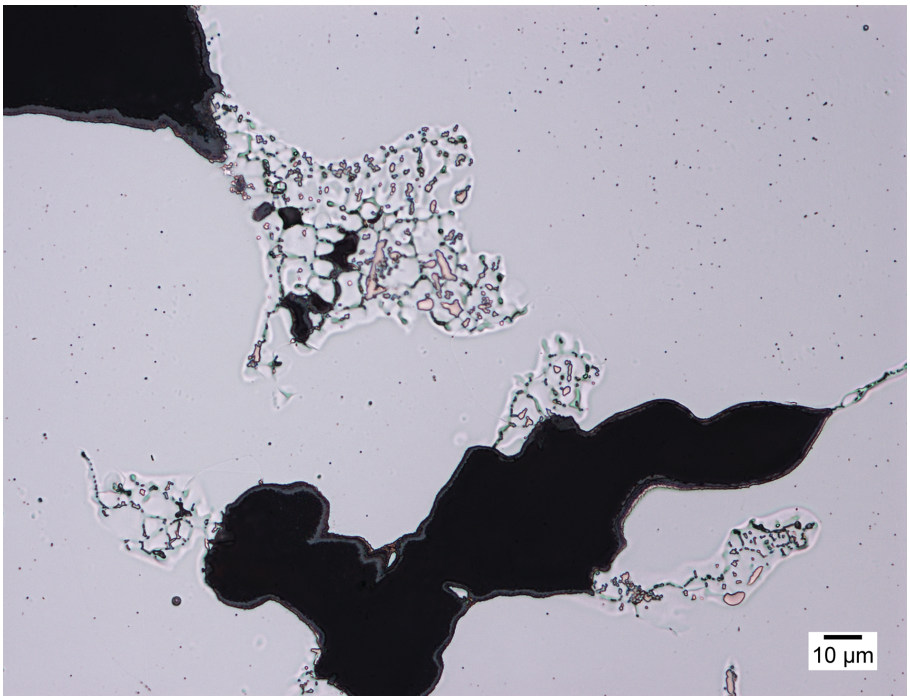

(b) 500X

Figure 5.17: Optical micrographs showing evidence of liquation around interdendritic phases near the fracture surface in the Cone 5 On-Heating 1302 °C (2375 °F) hot ductility sample. Etch: electrolytic 10% oxalic acid.

5.2.3 Characterization of On-Cooling Hot Ductility Tests

Cone 1 On-Cooling

The near-surface region of the Cone 1 On-Cooling 1260 °C (2300 °F) (C1 OC-2300) hot ductility sample is shown in Figure 5.18. As with the C1 OH-2375 test (Figure 5.11), cracking is readily apparent with the crack paths following the interdendritic boundaries, and a significant fraction of the intradendritic precipitates have dissolved. However, compared with the C1 OH-2375 sample, the C1 OC-2300 sample exhibits a much larger extent of prior liquid formation near the fracture surface, which is apparent in Figure 5.18 and also at higher magnification in Figure 5.19 (see arrows). In these micrographs, the prior liquid films are nearly continuous across the fracture surface. The greater extent of liquation is due to the longer duration of elevated temperature exposure for this sample, even though C1 OH-2375 and C1 OC-2300 experienced the same peak temperature (recall that the peak temperature for the on-cooling tests was chosen as the on-heating ZDT, equal to 1302 °C (2375 °F)). In the on-cooling tests, the sample spends a short though definite amount of time near the peak of the welding thermal cycle before being fractured on-cooling, with the precise time dependent on the welding parameters and corresponding thermal cycle characteristics (for the thermal cycle utilized herein, the time near the peak corresponds to 1.4 s above 1293 °C (2360 °F)). In comparison, the on-heating ZDT sample (C1 OH-2375) was

fractured immediately upon reaching the peak temperature with correspondingly less time for liquid formation.

Figure 5.20 presents a higher magnification view of the region near the tip of the crack shown in Figure 5.18. Extensive liquated regions are apparent around the interdendritic phases and along the crack faces. The crack tip region is shown in the SEM micrographs in Figure 5.21, with the corresponding EDXS analysis results (from the box in Figure 5.21b) given in Figure 5.22. There are numerous small particles located on the crack faces and on the interdendritic boundary ahead of the crack tip, which are enriched in Nb (Figure 5.22); the Fe, Cr, and Ni peaks originate from the surrounding matrix. Notably, Si enrichment above the nominal alloy composition is not observed which indicates that the Ni-Nb-Si phase is not present in the interdendritic region depicted here.

The liquated region surrounding some of the interdendritic phases in Figure 5.18 is evaluated further in the SEM micrographs in Figure 5.23 with corresponding EDXS spot analysis results in Figure 5.24. The quantitative EDXS results indicate that the white particle is NbC while the surrounding prior liquid (around the interdendritic phases) is essentially similar to the nominal alloy composition and is not enriched in Ni or Si, indicating that the formation of prior liquid in this region (along the interdendritic boundaries) is not due to melting of Ni-Nb-Si phases during the simulated on-cooling thermal cycle. However, as in the C1 OH-2375 sample, a small level of Nb was detected in the prior liquid region.

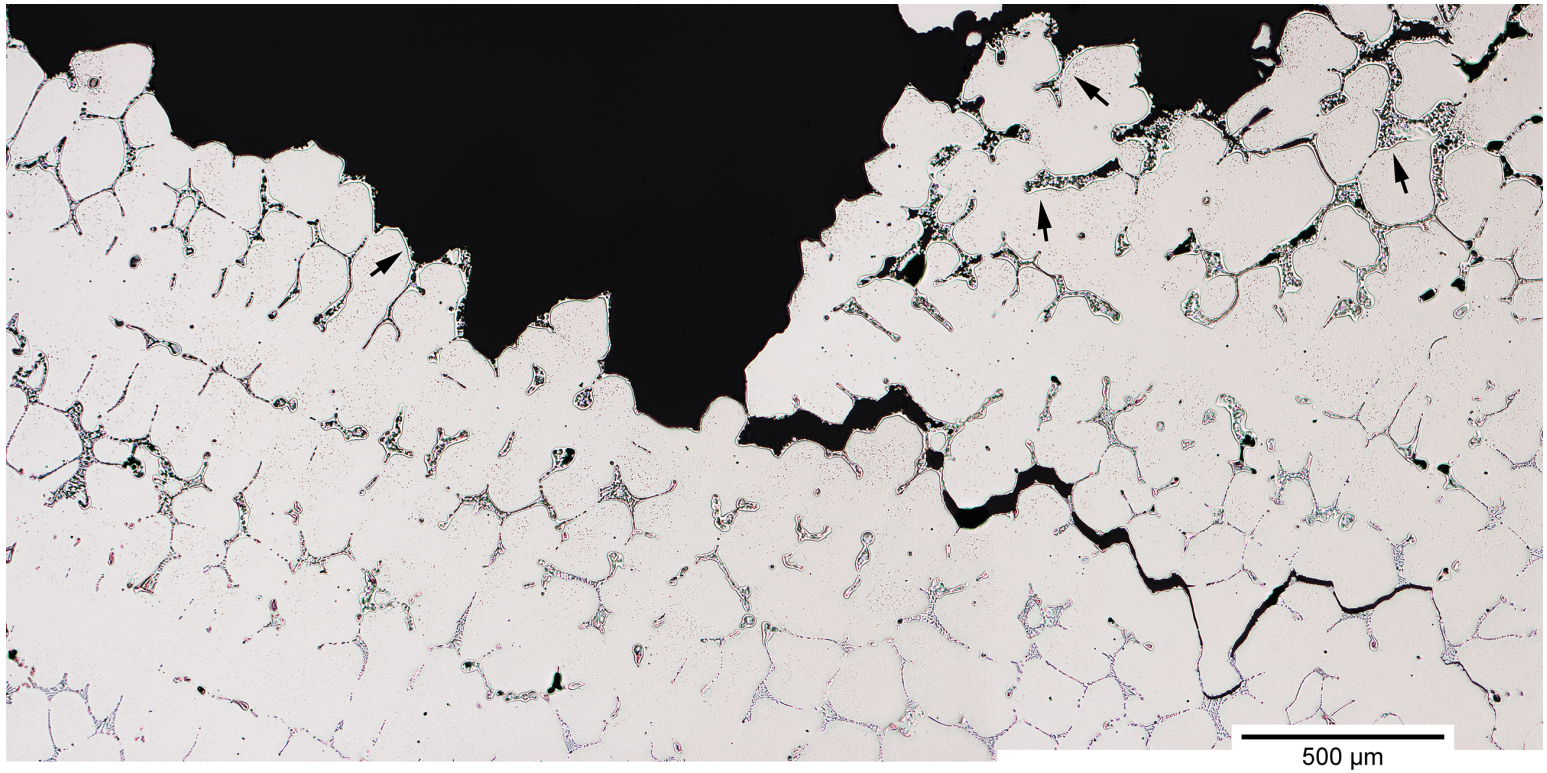

Figure 5.18: Optical micrograph of a region of the fracture surface in the Cone 1 On-Cooling 1260 °C (2300 °F) hot ductility sample. Note the extensive formation of liquated regions near the surface (e.g. as denoted by arrows). Original magnification, 50X. Etch: electrolytic 10% oxalic acid.

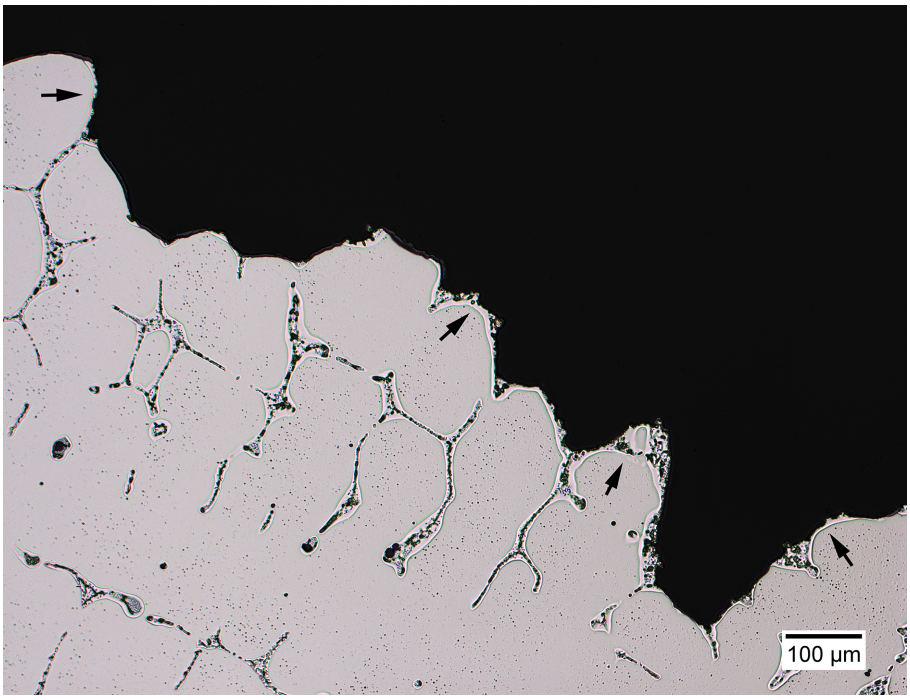

Figure 5.19: Optical micrograph showing a nearly continuous film of prior liquid (arrows) along the fracture surface of the Cone 1 On-Cooling 1260 °C (2300 °F) hot ductility sample, 100X. Etch: electrolytic 10% oxalic acid.

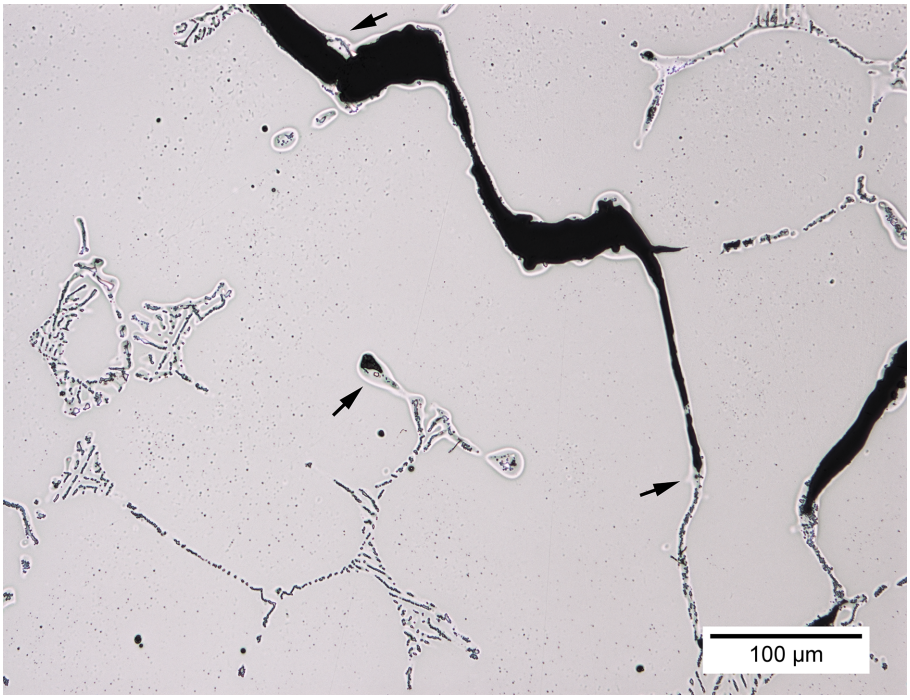

Figure 5.20: Optical micrograph showing extensive liquation (arrows) along the crack faces and surrounding interdendritic phases, near the tip of the crack visible in Figure 5.18 for the Cone 1 On-Cooling 1260 °C (2300 °F) hot ductility sample, 200X. Etch: electrolytic 10% oxalic acid.

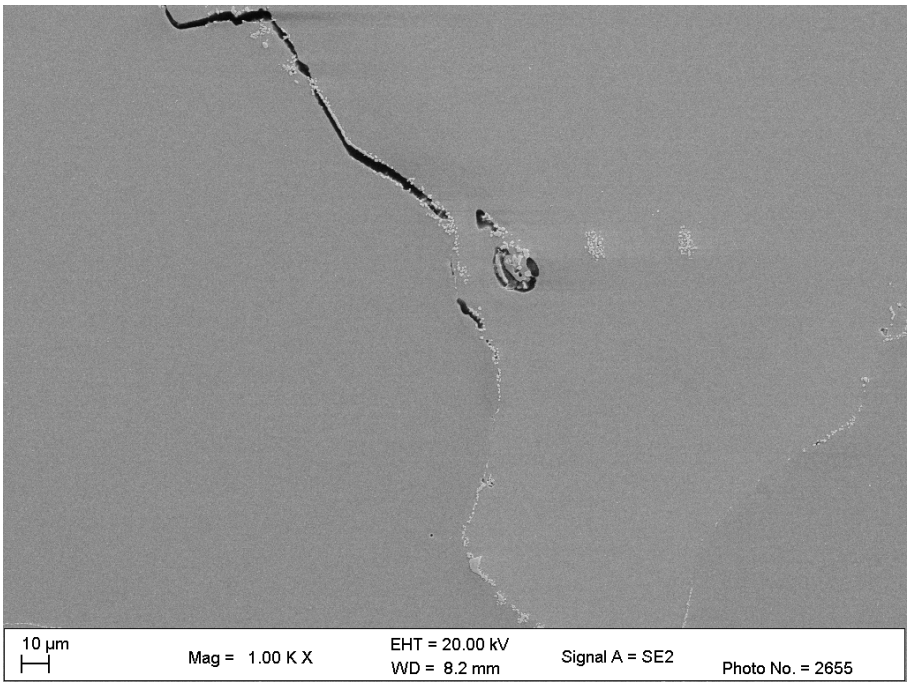

(a) 1000X

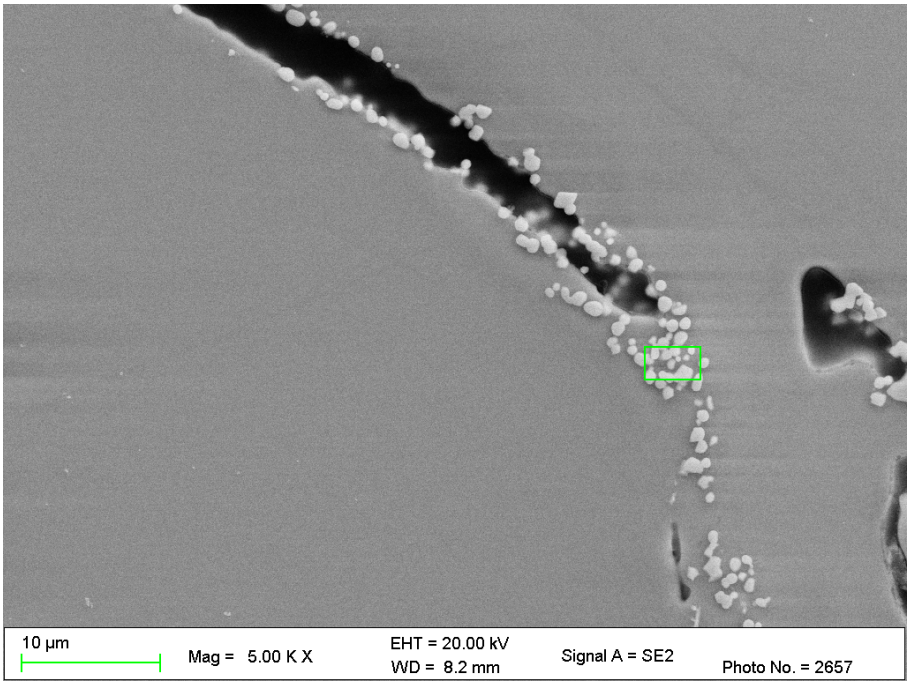

(b) 5000X

Figure 5.21: SEM micrographs showing the region at the tip of the crack visible in Figure 5.18 for the Cone 1 On-Cooling 1260 °C (2300 °F) hot ductility sample. The EDXS results for the boxed area in (b) are given in Figure 5.22. Etch: electrolytic 10% oxalic acid.

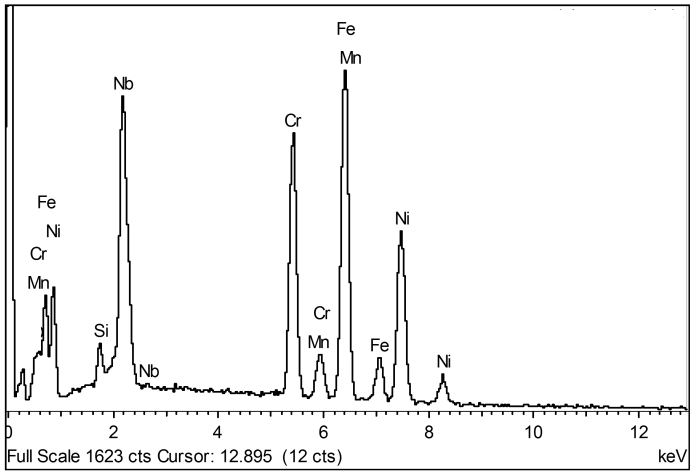

Element	Analysis (wt. %)	Analysis (at. %)
Nb	21	14
Cr	18	20
Fe	33	35
Ni	26	26
Mn	1.2	1.3
Si	1.3	3

Figure 5.22: EDXS results for the boxed area shown in Figure 5.21b for the Cone 1 On-Cooling 1260 °C (2300 °F) hot ductility sample , at the tip of the crack.

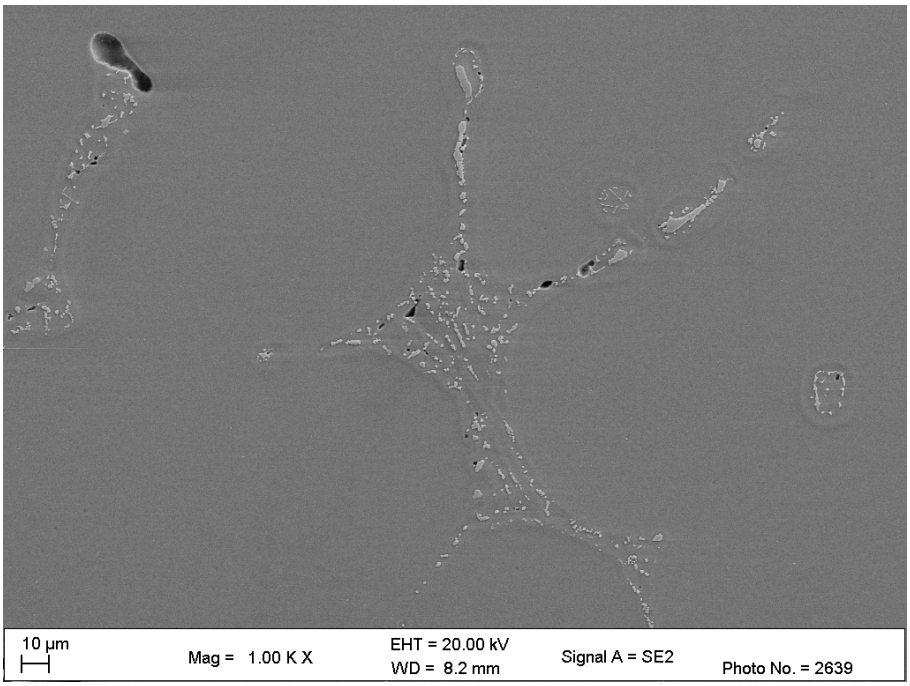

(a) 1000X

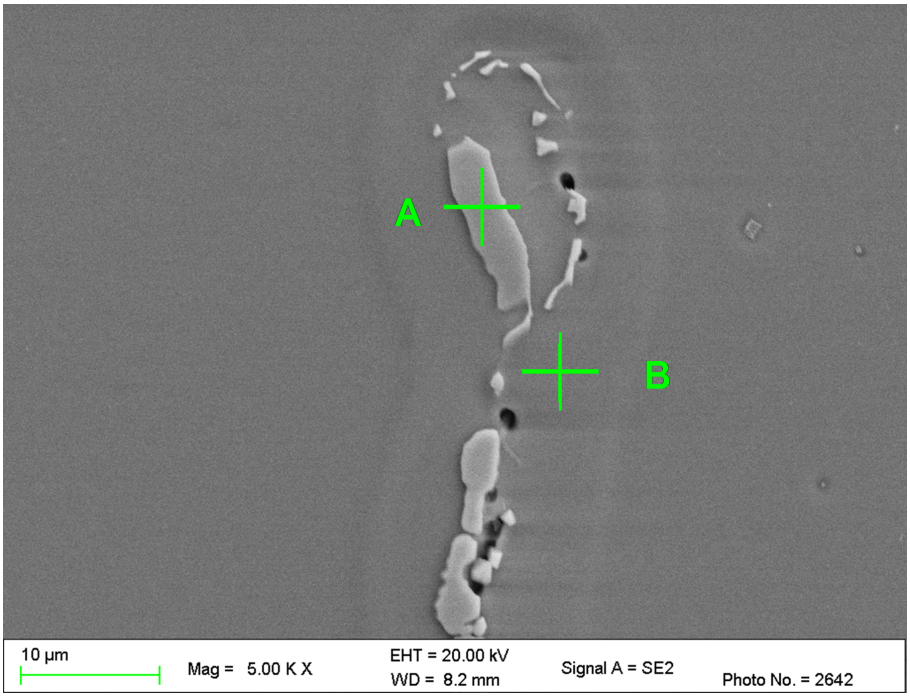

(b) 5000X

Figure 5.23: SEM micrographs showing evidence of liquation around interdendritic phases adjacent to the fracture surface in the Cone 1 On-Cooling 1260 °C (2300 °F) hot ductility sample. EDXS spot analysis results for the indicated points "A" and "B" in (b) are given in Figure 5.24.

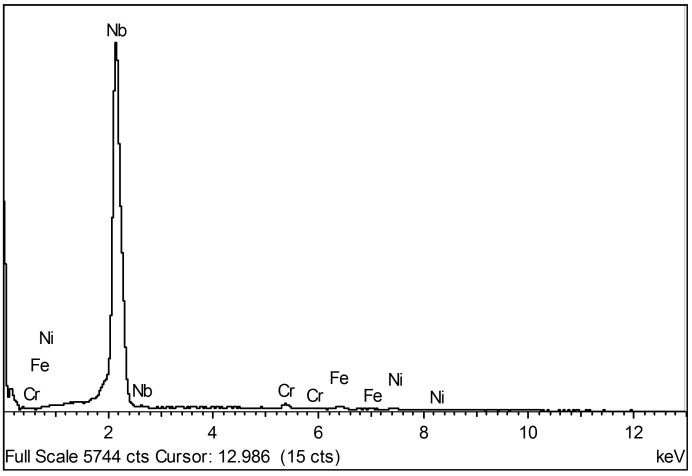

Element	Analysis (wt. %)	Analysis (at. %)
Nb	96	94
Cr	1.5	3
Fe	1.4	2
Ni	0.8	1

(a) Spot EDXS results for point "A"

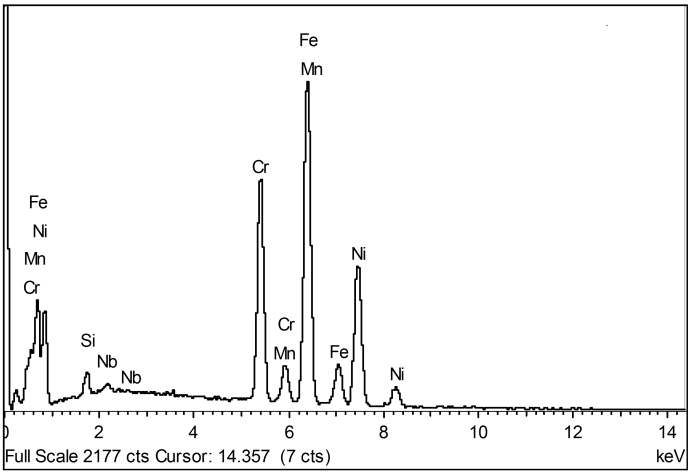

Element	Analysis (wt. %)	Analysis (at. %)
Cr	21	22
Ni	32	30
Fe	45	44
Mn	1	1
Si	1	2
Nb	0.8	0.5

(b) Spot EDXS results for point "B"

Figure 5.24: Spot EDXS results for the indicated points "A" and "B" in Figure 5.23b for the Cone 1 On-Cooling 1260 °C (2300 °F) hot ductility sample.

Cone 5 On-Cooling

Figure 5.25 shows a region adjacent to the fracture surface of the Cone 5 On-Cooling 1260 °C (2300 °F) (C5 OC-2300) hot ductility sample. As with the C1 OC-2300 sample, C5 OC-2300 shows significant cracking along the interdendritic boundaries, with the cracked portions of the boundaries generally oriented perpendicular to the tensile loading direction. Extensive liquation is also apparent in Figure 5.25, both along the edge of the fracture profile and around the interdendritic phases slightly away from fracture. The extent of prior liquid formed is similar to the C1 OC-2300 sample and as in that case, the greater extent of liquid formation compared to the on-heating test (C5 OH-2375) is due to the longer exposure to the peak temperature of the simulated thermal cycle. The tip of the larger crack, from Figure 5.25, is shown at higher magnification in Figure 5.26, where liquation is evident around the interdendritic boundary ahead of the crack as well as nearby secondary phases (denoted by arrows). The tip of the crack was examined in the SEM as shown in Figure 5.27. The compositions of the indicated points in Figure 5.27b, corresponding to the liquated region around the crack and a nearby particle, are shown in Figure 5.28 as determined by EDXS. The liquated region near the crack tip shows essentially the nominal alloy composition and does not reveal Ni or Si enrichment, although a small amount of Nb is present. The particle (whitish in appearance) is shown to be enriched in Nb (29 wt.%) and thus most likely a niobium carbide, with other peaks including Cr, Fe, and Ni (with

amounts near the nominal alloy composition) in the spectrum originating from the surrounding matrix.

Another liquated region near the fracture surface is shown in the optical micrographs in Figure 5.29. A significant extent of prior liquid formation is evident surrounding a region with a eutectic-like structure. The boxed region in Figure 5.29b is examined at higher magnification in the SEM micrographs (obtained using BSE imaging mode) presented in Figure 5.30. The EDXS results for the indicated points are given in Figure 5.31. Point "A" corresponds to the prior liquid and shows a composition close to the nominal alloy composition, but with a small amount of Nb (similar to the prior liquid regions in the C1 OH-2375 and C1 OC-2300 samples). In comparison, Nb is not detected at an adjacent location in the matrix (outside of the prior liquid) as indicated by point "B". It is apparent from Figure 5.27b that the phases (highlighted by arrows) at points "C" and "D" have a different appearance from the surrounding brighter "white"-appearing particles (which are NbC), resulting from the chemical composition contrast provided by BSE imaging. Both phases analyzed at points "C" and "D" are enriched in Si, Ni, and Nb compared to the nominal alloy composition. However, the EDXS compositions are not close to that of G-phase ($Ni_{16}Nb_6Si_7$) which has a composition of 55.8 wt.% Ni, 32.9 wt.% Nb, and 11.6 wt.% Si [21]. Furthermore, these phases were present only to an extremely minimal extent in the C5 OC-2300 sample and were isolated in distribution, indicating that these Ni-Nb-Si enriched phases (which do not appear to correspond to G-phase) could not significantly contribute

to the observed liquation along the interdendritic boundaries. Considering the presence of Nb in the prior liquid regions (both in on-heating and on-cooling samples) and observed eutectic-like structures containing NbC in conjunction with solidified liquid (e.g. Figure 5.29), a constitutional liquation reaction between NbC and austenite, due to rapid heating during the simulated thermal cycle, is likely responsible for the observed liquation along the interdendritic boundaries with subsequent formation of a NbC-austenite eutectic upon resolidification. This behavior has been observed in other niobium-containing materials; Lee [28] investigated the hot ductility behavior of 347NG (nuclear grade) stainless steel, which is niobium stabilized and contains NbC carbides, and observed NbC-austenite eutectic constituents associated with constitutional liquation along grain boundaries.

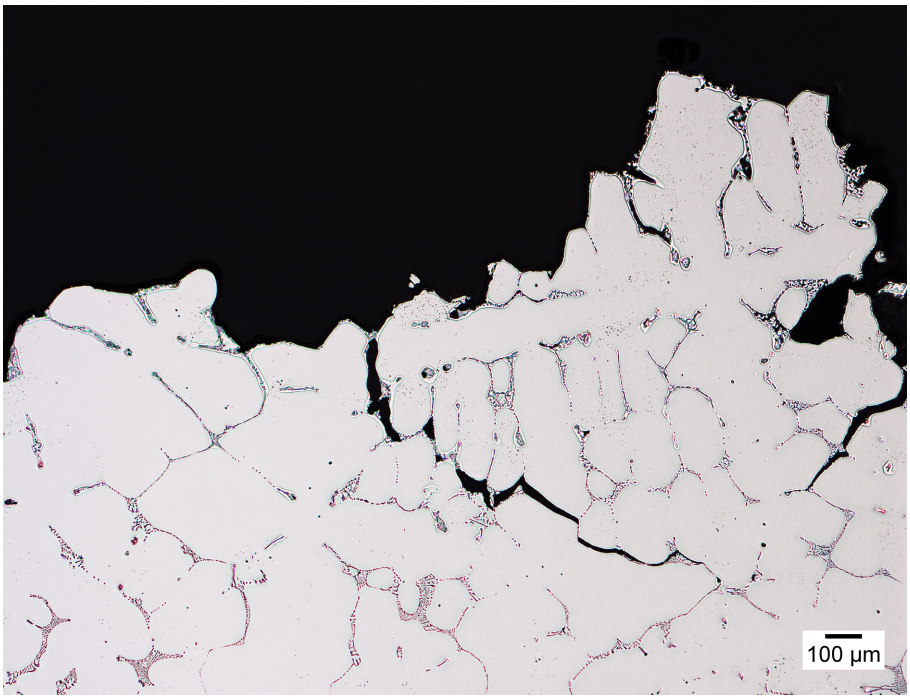

Figure 5.25: Optical micrograph showing a region adjacent to the fracture surface in the Cone 5 On-Cooling 1260 °C (2300 °F) hot ductility sample, 50X. Etch: electrolytic 10% oxalic acid.

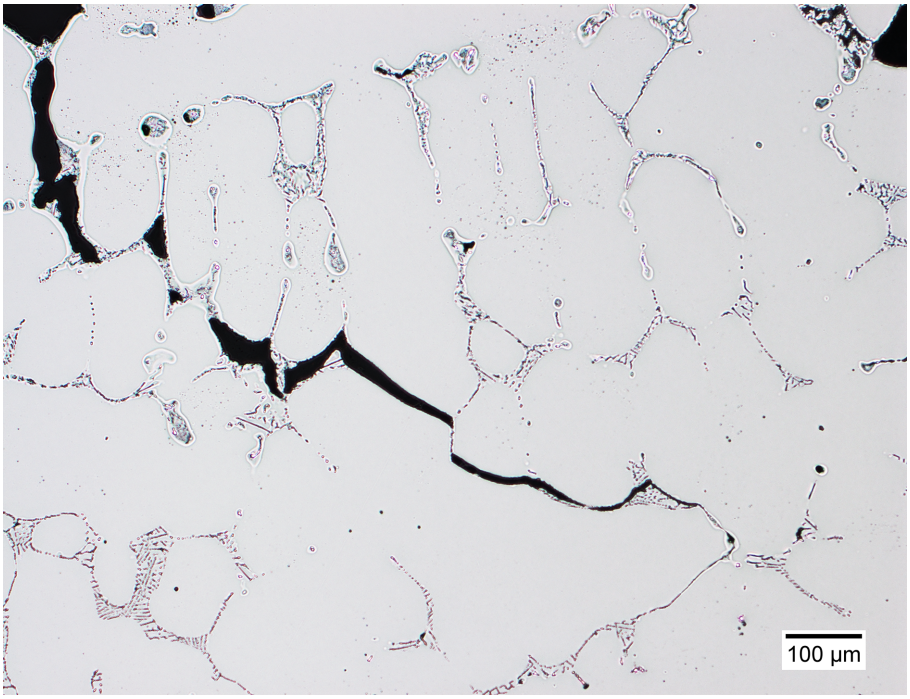

(a) 100X

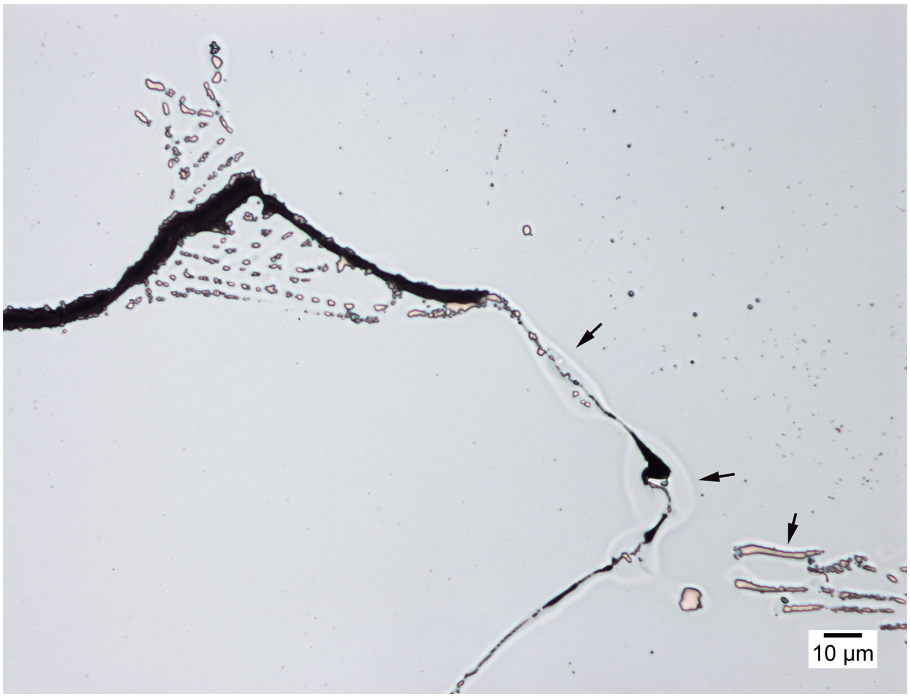

(b) 500X

Figure 5.26: Optical micrographs showing the crack visible in Figure 5.25 for the Cone 5 On-Cooling 1260 °C (2300 °F) hot ductility sample. Liquated regions around the crack tip and interdendritic phases are denoted by arrows. Etch: electrolytic 10% oxalic acid.

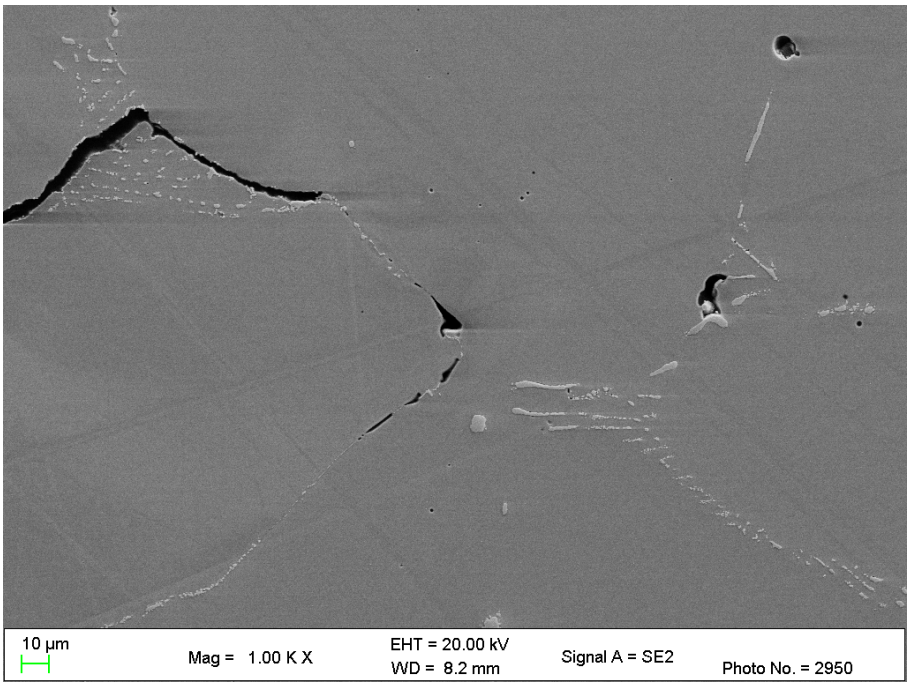

(a) 1000X

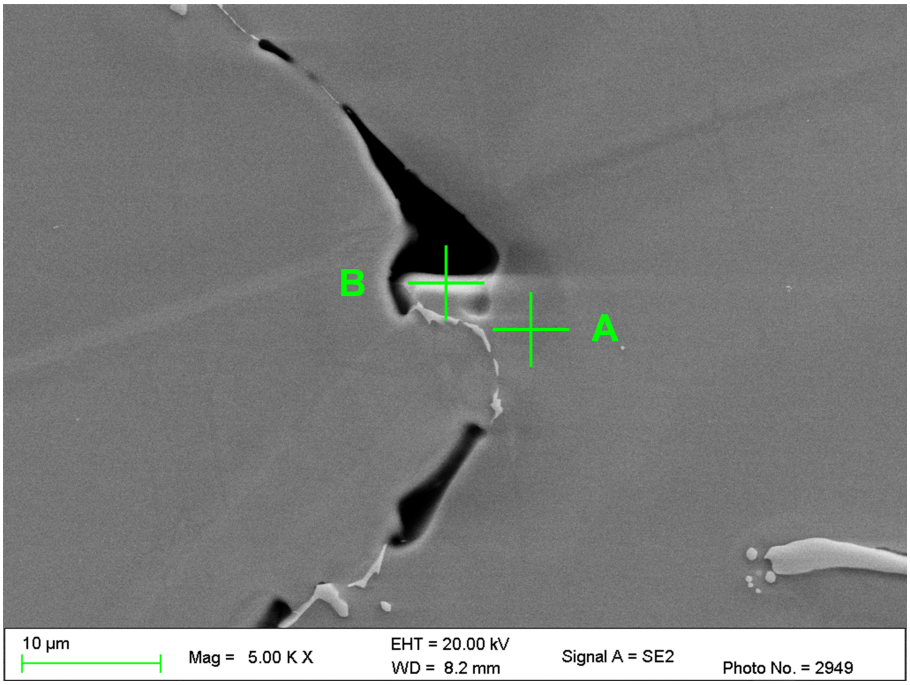

(b) 5000X

Figure 5.27: SEM micrographs of a crack tip region (cf. Figure 5.26) in the Cone 5 On-Cooling 1260 °C (2300 °F) hot ductility sample. The EDXS results for the indicated points "A" and "B" are given in Figure 5.28. Etch: electrolytic 10% oxalic acid.

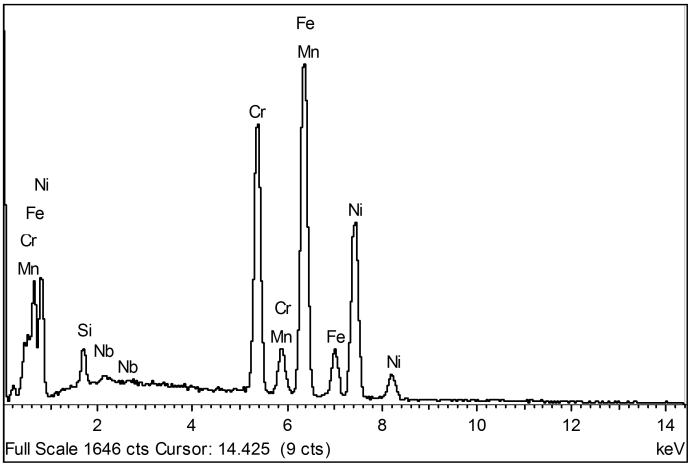

Element	Analysis (wt. %)	Analysis (at. %)
Cr	21	22
Ni	33	31
Fe	43	42
Si	1.2	2.4
Mn	1.9	1.9
Nb	0.7	0.4

(a) Spot EDXS results for point "A"

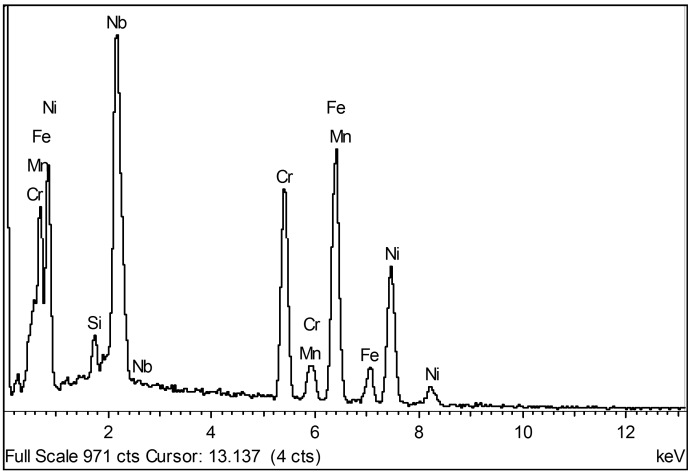

Element	Analysis (wt. %)	Analysis (at. %)
Cr	17	21
Ni	23	24
Fe	29	32
Mn	1.2	1.4
Si	1.7	3.7
Nb	29	19

(b) Spot EDXS results for point "B"

Figure 5.28: Spot EDXS results for indicated points "A" and "B" in Figure 5.27 at a crack tip region in the Cone 5 On-Cooling 1260 °C (2300 °F) hot ductility sample.

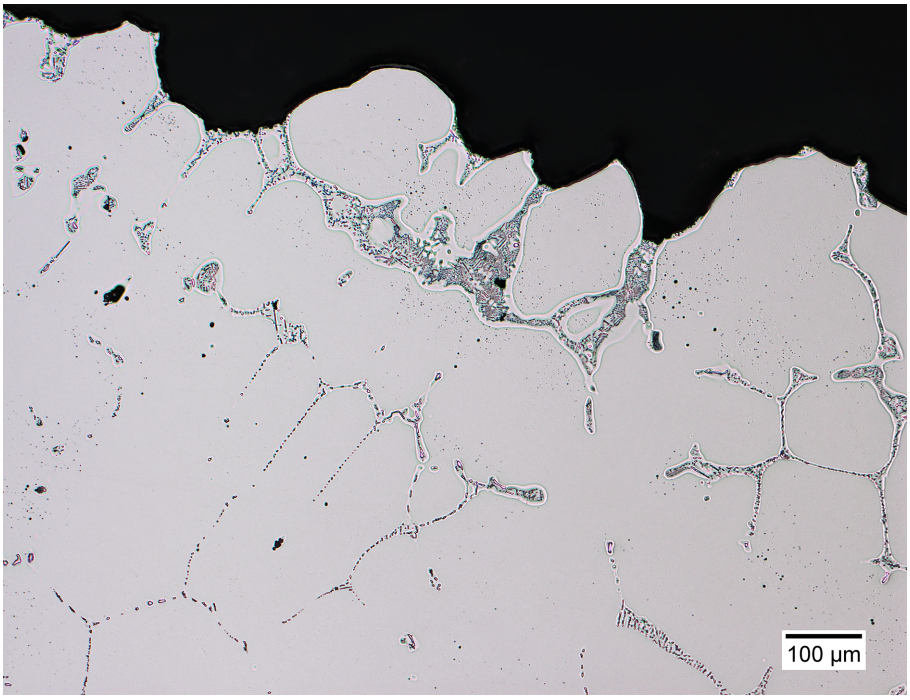

(a) 100X

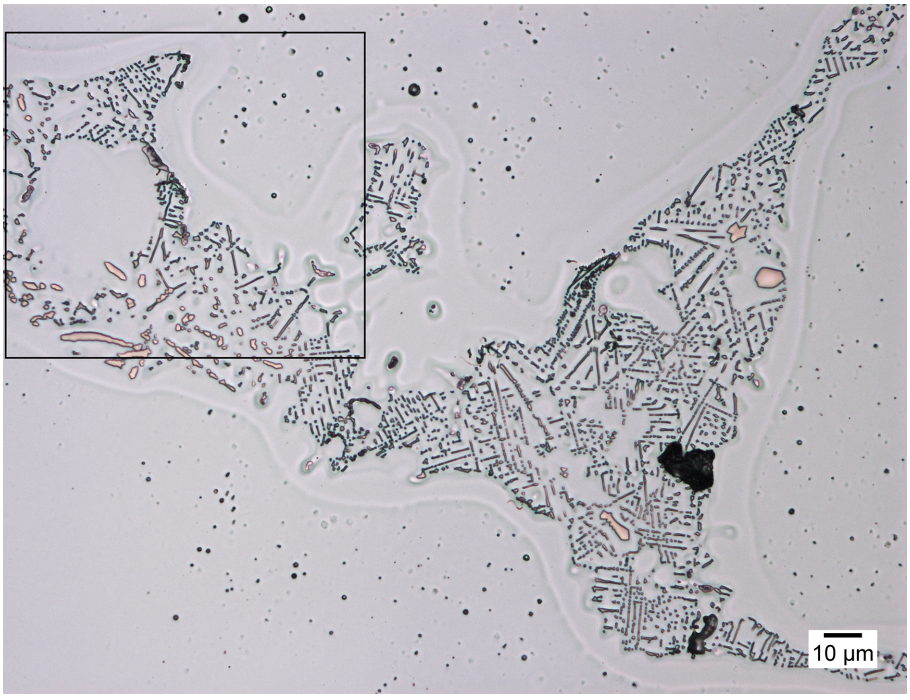

(b) 500X

Figure 5.29: Optical micrographs showing a liquated region adjacent to the fracture surface in the Cone 5 On-Cooling 1260 °C (2300 °F) hot ductility sample. The boxed region in (b) is examined at higher magnification in Figure 5.30. Etch: electrolytic 10% oxalic acid.

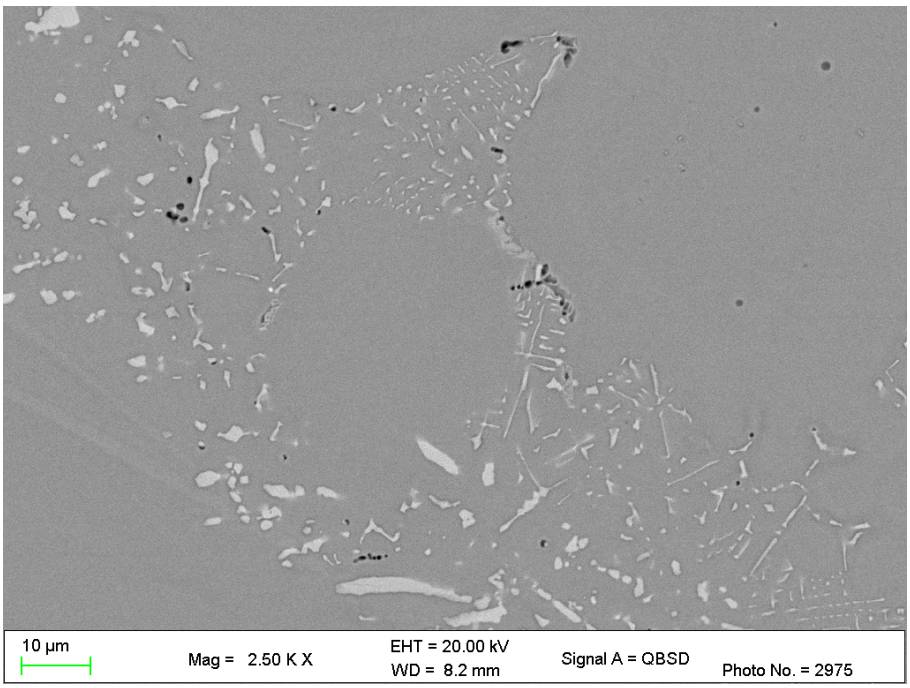

(a) 2500X

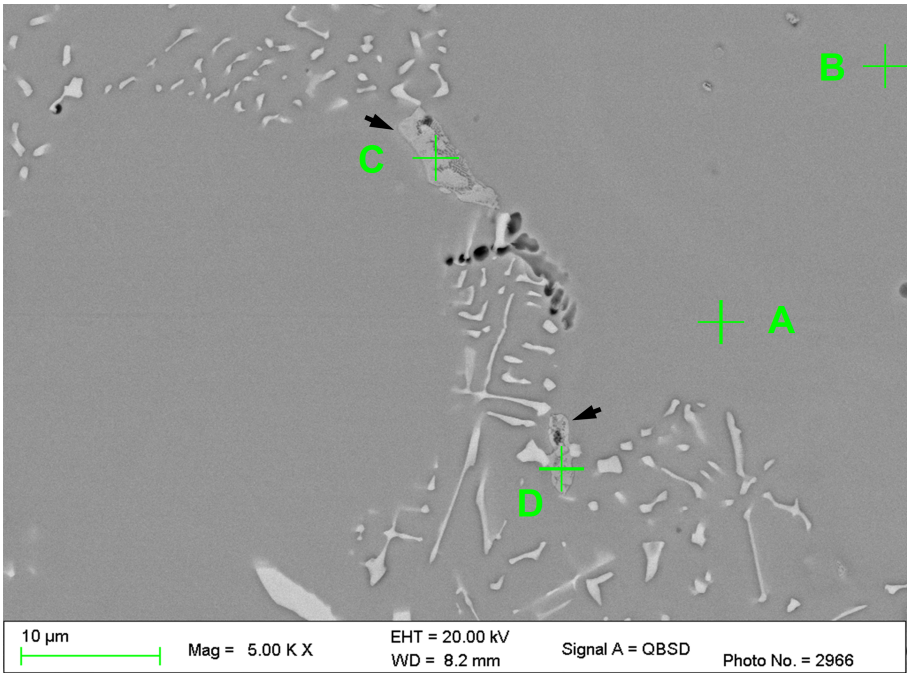

(b) 5000X

Figure 5.30: BSE-SEM micrographs of the boxed region from Figure 5.29 showing liquation surrounding interdendritic phases in the Cone 5 On-Cooling 1260 °C (2300 °F) hot ductility sample. EDXS results for the indicated points in (b) are given in Figure 5.31. Etch: electrolytic 10% oxalic acid.

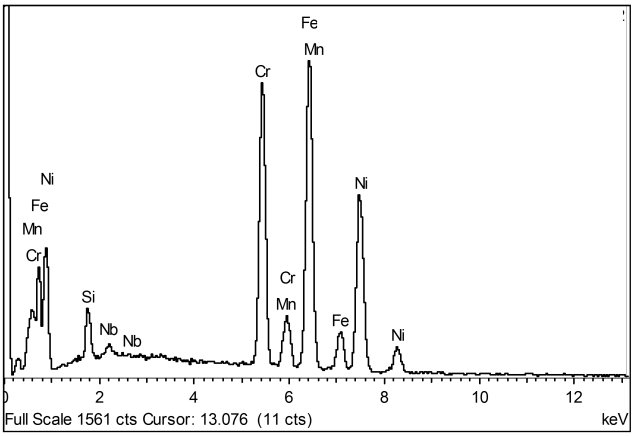

Element	Analysis (wt. %)	Analysis (at. %)
Cr	19	21
Ni	32	30
Fe	46	45
Mn	1.4	1.4
Si	1	2
Nb	1	0.5

(a) Spot EDXS results for point "A" (corresponding to prior liquid in Figure 5.30b)

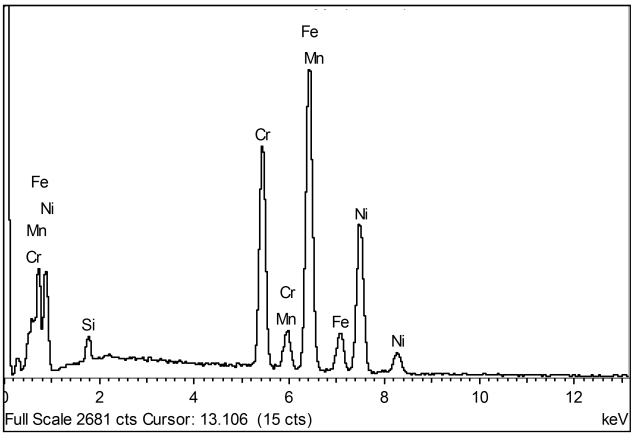

Element	Analysis (wt. %)	Analysis (at. %)
Cr	21	23
Ni	33	31
Fe	43	43
Mn	1.2	1.2
Si	1.4	2.8

(b) Spot EDXS results for point "B" (corresponding to matrix in Figure 5.30b)

Figure 5.31: Spot EDXS results for indicated points "A", "B", "C", and "D" in Figure 5.30 at a liquated region in the Cone 5 On-Cooling 1260 °C (2300 °F) hot ductility sample.

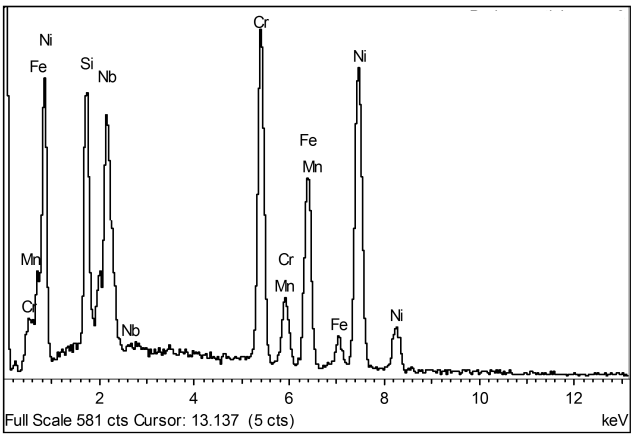

Element	Analysis (wt. %)	Analysis (at. %)
Cr	20	22
Ni	40	37
Fe	16	16
Mn	1.6	1.6
Si	8.3	16
Nb	14	8

(c) Spot EDXS results for point "C"

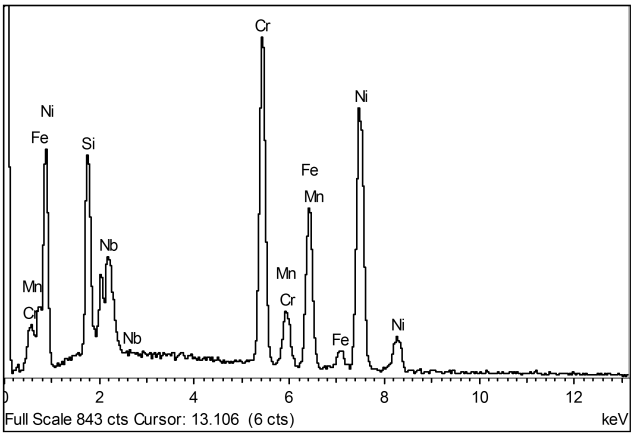

Element	Analysis (wt. %)	Analysis (at. %)
Cr	24	24
Ni	44	39
Fe	16	16
Mn	2	2
Si	9	17
Nb	5	3

(d) Spot EDXS results for point "D"

Figure 5.31: (cont.) Spot EDXS results for indicated points "A", "B", "C", and "D" in Figure 5.30 at a liquated region in the Cone 5 On-Cooling 1260 °C (2300 °F) hot ductility sample.

Chapter 6

Conclusions

Two centrifugally-cast, 20Cr-32Ni-1Nb hydrogen reformer outlet manifold components were evaluated using the Gleeble® hot ductility test to determine the potential susceptibility to HAZ liquation cracking. The evaluation revealed the following:

1. Both 20Cr-32Ni-1Nb heats (Cone 1 and Cone 5) exhibited similar as-received microstructures, with numerous NbC carbides along the interdendritic boundaries. A significant extent of fine intradendritic precipitates was also observed in the as-received material. However, evidence of Ni-Nb-Si enriched phases adjoining the interdendritic NbC, commonly reported for service-exposed ("aged") 20Cr-32Ni-1Nb material, was not observed. Thus, it is

likely that both materials in the current study were subjected to a solution-annealing treatment after removal from service, contrary to the initial information provided with the materials.

2. Both Cone 1 and Cone 5 exhibited Class H1 hot ductility behavior when tested on-heating, with an on-heating ZDT of 1302 °C (2375 °F). Class H1 on-heating behavior is not, in and of itself, indicative of high sensitivity to liquation cracking.

3. Based on the Nippes criteria, both Cone materials exhibited Class C3 behavior when tested upon cooling from a peak temperature equal to the ZDT. Class C3 behavior corresponds to a generally poor recovery of on-cooling ductility after exposure to the HAZ peak temperature. This classification of the Cone 1 and Cone 5 on-cooling behavior was further corroborated by observed ZDRs of 24 C° (75 F°) and calculated DRR values on the order of 20% at 1218 °C (2225 °F) for both Cone materials.

4. On the basis of the observed Class H1/Class C3 behavior together with the determined values of the ZDR and DRR criteria, the Cone 1 and Cone 5 materials were shown to be sensitive to liquation cracking in the base metal HAZ. Furthermore, considering the likelihood that both the Cone 1 and Cone 5 materials were in the solution-annealed condition, the liquation cracking susceptibility of service-exposed material is expected to be on a similar, or more likely higher, level. In any case, hot ductility testing during

the early stages of development of the 20Cr-32Ni-1Nb alloy would have revealed the susceptibility to liquation cracking and this information would have been valuable for avoiding the repair welding problems experienced by industry.

5. The Cone 1 and Cone 5 hot ductility samples tested on-heating at 1302 °C (2375 °F) showed similar microstructures exhibiting cracking along the interdendritic boundaries decorated with NbC and dissolution of fine intradendritic precipitates near the fracture surface. At this test temperature, corresponding to the ZDT, the beginning of liquation at some interdendritic boundaries was apparent, and this liquation was the cause of the observed zero ductility behavior at this temperature.

6. In the Cone 1 and Cone 5 hot ductility samples tested on-cooling at 1260 °C (2300 °F) after exposure to the ZDT, cracking along the interdendritic boundaries near the fracture surface was again observed accompanied by dissolution of fine intradendritic precipitates. Compared to the on-heating tests, a significantly greater extent of liquation around crack faces and interdendritic phases was apparent, due to longer exposure time near the peak temperature of the simulated thermal cycle (longer time near the ZDT). The extensive liquation was responsible for the observed zero ductility behavior at the DRT.

7. In all of the on-heating and on-cooling hot ductility samples, the composition of the prior liquid present at liquated boundaries was similar to the nominal

alloy composition except for the presence of small amounts of Nb. In particular, the prior liquid regions did not show evidence of Ni or Si enrichment, which indicates that incipient melting of Ni-Nb-Si enriched phases (G-phase) was not responsible for the observed liquation.

8. Due to the low extent (nearly zero) of Ni-Nb-Si enriched phases in both the as-received materials and tested hot ductility samples, together with the presence of Nb in the prior liquid regions, the observed liquation of interdendritic boundaries at temperatures below the bulk solidus temperature was attributed to constitutional liquation of NbC located on the boundaries.

Chapter 7

Future Work

The hot ductility behavior of modified chemistry heats of 20Cr-32Ni-1Nb, created with the goal of reducing the formation of Ni-Nb silicide phases upon service exposure, should be investigated to determine if the modified chemistry alloys are effective in improving the repair weldability in the service-exposed condition. For example, the modified chemistry 20Cr-32Ni-1Nb alloy evaluated by Hoffman and Magnan [46], in which the Si content was reduced and the Nb content was also reduced to a level below the stoichiometric Nb/C ratio of 7.7, was shown to decrease the formation of Ni-Nb silicides after long-term aging with concomitant improvements in tensile properties. Dewar and Gerlich [45] used a thermodynamic approach to investigate the effects of nitrogen additions to 20Cr-32Ni-1Nb and found that nitrogen decreased the fraction of G-phase and lowered the G-phase stability temperature. While these changes appear promising, weldability testing together with microstructural evaluation must be conducted to

verify whether the chemistry modifications are actually effective in reducing the propensity for HAZ liquation cracking during repair welding.

Weldability evaluation of cast tee materials should also be performed to quantify the cracking propensity of statically cast materials (with potentially larger grain size and greater formation of secondary phases). Hoffman [21] observed that statically cast tee materials exhibited a greater reduction in tensile properties after service exposure than centrifugally cast cones. This behavior suggests that statically cast materials may show a greater susceptibility to liquation cracking upon repair welding, which should be investigated through hot ductility testing.

Bibliography

[1] J. R. Rostrup-Nielsen, "Catalytic Steam Reforming", in *Catalysis*, ser. Catalysis: Science and Technology, J. R. Anderson and M. Boudart, Eds., vol. 5, Berlin, Heidelberg: Springer-Verlag, Jan. 1, 1984, pp. 1–117, ISBN: 978-3-642-93249-6. [Online]. Available: http://dx.doi.org/10.1007/978-3-642-93247-2_1.

[2] P. Häussinger, R. Lohmüller, and A. M. Watson, "Hydrogen", in *Ullmann's Encyclopedia of Industrial Chemistry*, Wiley-VCH Verlag GmbH & Co. KGaA, 2000, ISBN: 978-3-527-30673-2. [Online]. Available: http://onlinelibrary.wiley.com.proxy.lib.utk.edu:90/doi/10.1002/14356007.o13_o03/abstract.

[3] J. Penso and H. Mead, "Repair case histories and mitigation of cast 20-32 Nb reducers", API Roundtable Discussion, Issues with Alloys in Hydrogen Furnaces, API Spring Refining and Equipment Standards Meeting, Dallas, May 2006.

[4] C. M. Schillmoller, "HP-Modified furnace tubes for steam reformers and steam crackers", Nickel Development Institute, NiDI Technical Series 10 058, Apr. 1992.

[5] T. Shibasaki, T. Mohri, and K. Takemura, "Experience with cast material for steam reformer furnaces", in *Proceedings of Ammonia Plant Safety & Related Facilities Symposium*, Paper no. 3a, vol. 34, Orlando, FL: American Institute of Chemical Engineers, 1994, pp. 166–176.

[6] P. A. Collins, "Effect of elevated temperature exposure on the mechanical properties of a cast niobium-containing alloy", in *Proceedings of the International Corrosion Forum Devoted Exclusively to the Protection and Performance of Materials*, Paper no. 170, Chicago, IL: NACE International, Mar. 3–7, 1980.

[7] "ASTM A351/A351M-10, Standard Specification for Castings, Austenitic, for Pressure-Containing Parts", ASTM International, West Conshohocken, PA, 2010.

[8] "Materials, fabrication, and repair considerations for hydrogen reformer furnace outlet pigtails and manifolds", American Petroleum Institute, Technical Report 942-A, Jun. 2014.

[9] J. J. Hoffman and R. L. Colwell, "Weld cracking in Nb modified heat resistant castings: A microstructural investigation", in *Corrosion 98*, Paper 423, NACE International, 1998.

[10] M. Blair, "Cast stainless steels", in *Properties and selection: Irons, steels, and high-performance alloys*, ser. ASM Handbook, 10th ed., vol. 1, ASM International, 1990, pp. 908–929. [Online]. Available: products.asminternational.org/hbk/index.jsp.

[11] "Metallurgy and properties of cast stainless steels", in *Stainless Steels*, ser. ASM Specialty Handbook, J. Davis, Ed., ASM International, 1994.

[12] H. S. Avery, "Cast heat-resistant alloys for high-temperature weldments", Welding Research Council, Bulletin 143, Aug. 1969.

[13] R. H. Kane, "The evolution of high temperature alloys: A designer's perspective", in *Heat-Resistant Materials: PROCEEDINGS of the First International Conference*, Lake Geneva, WI: ASM International, 1991, pp. 1–8.

[14] E. Folkhard, *Welding metallurgy of stainless steels*. Springer-Verlag, 1988.

[15] T. Sourmail, "Precipitation in creep resistant austenitic stainless steels", *Materials Science and Technology*, vol. 17, no. 1, pp. 1–14, Jan. 2001, ISSN: 0267-0836, 1743-2847. DOI: 10.1179/026708301101508972. [Online]. Available: http://www.maneyonline.com/doi/abs/10.1179/026708301101508972.

[16] S. R. Keown and F. B. Pickering, "Niobium in stainless steels", presented at the International Symposium Niobium 1981, San Francisco, USA, 1981, pp. 1113–1141.

[17] G. D. de Almeida Soares, L. H. de Almeida, T. L. da Silveira, and I. Le May, "Niobium additions in HP heat-resistant cast stainless steels", *Materials Characterization*, vol. 29, no. 3, pp. 387–396, Oct. 1992, ISSN: 1044-5803. DOI: 10.1016/1044-5803(92)90045-J. [Online]. Available: http://www.sciencedirect.com/science/article/pii/104458039290045J.

[18] Q. Chen, C. Thomas, and D. Knowles, "Characterisation of 20Cr32Ni1Nb alloys in as-cast and Ex-Service conditions by SEM, TEM and EDX", *Materials Science and Engineering: A*, vol. 374, no. 1-2, pp. 398–408, Jun. 15,

2004, ISSN: 0921-5093. DOI: 10.1016/j.msea.2004.03.038. [Online]. Available: http://www.sciencedirect.com/science/article/pii/S0921509304003156.

[19] R. A. Pedro Ibañez, G. D. de Almeida Soares, L. H. de Almeida, and I. Le May, "Effects of Si content on the microstructure of modified-HP austenitic steels", *Materials Characterization*, vol. 30, no. 4, pp. 243–249, Jun. 1993, ISSN: 1044-5803. DOI: 10.1016/1044-5803(93)90071-3. [Online]. Available: http://www.sciencedirect.com/science/article/pii/1044580393900713.

[20] R. C. Ecob, R. C. Lobb, and V. L. Kohler, "The formation of G-phase in 20/25 Nb stainless steel AGR fuel cladding alloy and its effect on creep properties", *Journal of Materials Science*, vol. 22, no. 8, pp. 2867–2880, Aug. 1, 1987, ISSN: 0022-2461, 1573-4803. DOI: 10.1007/BF01086484. [Online]. Available: http://link.springer.com/article/10.1007/BF01086484.

[21] J. J. Hoffman, "High Temperature Aging Characteristics of 20Cr32Ni1Nb Castings", presented at the CORROSION 2000, Paper no. 00512, Orlando, FL: NACE International, Mar. 26, 2000. [Online]. Available: https://www.onepetro.org/conference-paper/NACE-00512.

[22] D. M. Knowles, C. W. Thomas, D. J. Keen, and Q. Z. Chen, "In service embrittlement of cast 20Cr32Ni1Nb components used in steam reformer applications", *International Journal of Pressure Vessels and Piping*, The 7th International Conference on Operating Pressure Equipment, vol. 81, no. 6, pp. 499–506, Jun. 2004, ISSN: 0308-0161. DOI: 10.1016/j.ijpvp.2003.12.025. [Online]. Available: http://www.sciencedirect.com/science/article/pii/S0308016103002187.

[23] J. C. Lippold, *Welding metallurgy and weldability*. Somerset, US: Wiley, 2014, ISBN: 978-1-118-96032-5.

[24] W. Yeniscavich, "Correlation of hot ductility curves with cracking during welding", in *Methods of High Alloy Weldability Evaluation*, New York, NY: Welding Research Council, Nov. 1970, pp. 2–12.

[25] J. J. Pepe and W. F. Savage, "Effects of constitutional liquation in 18-Ni maraging steel weldments", *Welding Journal*, vol. 46, no. 9, 411s–422s, Sep. 1967.

[26] J. Lippold, "Investigation of heat-affected zone hot cracking in Alloy 800", *Welding Journal*, vol. 62, no. 1, 1s–11s, 1983, ISSN: 00432296.

[27] B. Radhakrishnan and R. G. Thompson, "A phase diagram approach to study liquation cracking in alloy 718", *Metallurgical Transactions A*, vol. 22, no. 4, pp. 887–902, Apr. 1991, ISSN: 0360-2133, 1543-1940. DOI: 10.1007/BF02658999. [Online]. Available: http://link.springer.com/article/10.1007/BF02658999.

[28] C. H. Lee, "Weldability and microstructural analysis of nuclear grade austenitic stainless steels", PhD dissertation, University of Tennessee, Knoxville, Dec. 1988.

[29] "Standard welding terms and definitions", American Welding Society, Miami, FL, AWS Standard A3.0, 2010.

[30] J. C. M. Farrar, "Hot Cracking Tests — The Route to International Standardization", in *Hot Cracking Phenomena in Welds*, T. Böllinghaus and H. Herold, Eds., Springer Berlin Heidelberg, 2005, pp. 291–304, ISBN: 978-3-540-22332-0 978-3-540-27460-5. DOI: 10.1007/3-540-27460-X_15. [Online]. Available: http://link.springer.com/chapter/10.1007/3-540-27460-X_15.

[31] C. D. Lundin and W. F. Savage, "The Varestraint Test", *Welding Journal*, vol. 44, no. 10, 433s–442s, Oct. 1965.

[32] E. F. Nippes, W. F. Savage, B. J. Bastian, H. F. Mason, and R. M. Curran, "An investigation of the hot ductility of high temperature alloys", *Welding Journal*, vol. 34, no. 4, 183s–196s, Apr. 1955.

[33] E. F. Nippes, W. F. Savage, and L. L. Merrill, "Cooling rates in arc welds in 1/2 in. plate", *Welding Journal*, Research Supplement, vol. 28, no. 11, 556s–564s, Nov. 1949.

[34] E. F. Nippes and W. F. Savage, "Development of Specimens Simulating Weld Heat-Affected Zones", *Welding Journal*, Research Supplement, vol. 28, no. 11, 534s–546s, Nov. 1949.

[35] W. F. Savage, "Apparatus for studying the effects of rapid thermal cycles and high strain rates on the elevated temperature behavior of materials", *Journal of Applied Polymer Science*, vol. VI, no. 21, pp. 303–315, 1962.

[36] C. D. Lundin, "Historical development of the high-speed time-temperature controller designed for welding research: The Gleeble", in *Proceedings of 7th International Symposium on Physical Simulation*, Tsukuba, Japan, 1997.

[37] C. D. Lundin, C. Y. P. Qiao, and C. H. Lee, "Standardization of Gleeble hot ductility testing: Part I: Historical review", in *Weldability of Materials*, Detroit, USA: ASM International, 1990, pp. 1–8, ISBN: 0-87170-401-3.

[38] E. F. Nippes, W. F. Savage, and G. Grotke, "Further studies of the hot ductility of high temperature alloys", Welding Research Council, Bulletin 33, Feb. 1957, pp. 1–32.

[39] E. F. Nippes, H. Wawrousek, and W. L. Fleischmann, "The heat-affected zone in arc-welded Type 347 stainless steel", *Welding Journal*, vol. 34, no. 4, 169s–179s, Apr. 1955.

[40] "HAZ Software ver. 2.1 instruction manual for Gleeble 1500", Dynamic Systems, Inc., Nov. 1989.

[41] C. D. Lundin, C. Y. P. Qiao, and C. H. Lee, "Standardization of Gleeble hot ductility testing: Part II: Experimental evaluation", in *Weldability of Materials*, Detroit, USA: ASM International, 1990, pp. 9–22, ISBN: 0-87170-401-3.

[42] C. Y. Qiao, "Weldability of modified 800H alloys", PhD dissertation, University of Tennessee, Knoxville, Dec. 1993.

[43] S. Shi and J. Lippold, "Microstructure evolution during service exposure of two cast, heat-resisting stainless steels — HP–Nb modified and 20–32Nb", *Materials Characterization*, vol. 59, no. 8, pp. 1029–1040, Aug. 2008, ISSN: 1044-5803. DOI: 10.1016/j.matchar.2007.08.029. [Online]. Available: http://www.sciencedirect.com/science/article/pii/S1044580307003105.

[44] B. M. Patchett and R. W. Skwarok, "Welding metallurgy of 20Cr-32Ni-Nb and HP45 castings", *Materials for Resource Recovery and Transport*, pp. 379–390, 1998.

[45] M. P. Dewar and A. P. Gerlich, "Correlation between experimental and calculated phase fractions in aged 20Cr32Ni1Nb austenitic stainless steels containing nitrogen", *Metallurgical and Materials Transactions A*, vol. 44, no. 2, pp. 627–639, Feb. 1, 2013, ISSN: 1073-5623, 1543-1940. DOI: 10.1007/s11661-012-1457-1. [Online]. Available: http://link.springer.com/article/10.1007/s11661-012-1457-1.

[46] J. J. Hoffman and J. Magnan, "Cast 20Cr32Ni1Nb Alloy Aged Mechanical Property Improvements via Chemistry Modifications", presented at the CORROSION 2003, Paper no. 03469, NACE International, Jan. 1, 2003. [Online]. Available: https://www.onepetro.org/conference-paper/NACE-03469.

Vita

John Bohling was born in Visalia, CA to his parents, Mark and Sandra Bohling. He is the oldest of four sons. After a cross-country move with his family, John attended Auburn High School in Auburn, AL, and graduated in 2005. After working for a year, he enrolled at the University of Tennessee, Knoxville in the fall of 2006. He graduated with a Bachelor of Science in Materials Science and Engineering in December 2010. During his undergraduate studies, his classes on metallurgy and welding sparked his interest in these areas, and the following year, he started his graduate studies at the University of Tennessee with Dr. Carl Lundin in the area of materials joining and welding metallurgy. John graduated with his Master of Science in Materials Science and Engineering, with a concentration in metallurgy, in August 2016. He is continuing his graduate work with Dr. Lundin at the University of Tennessee for a Ph.D. in Materials Science and Engineering.